Article

N^1-Methylpseudouridine directly modulates translation dynamics

https://doi.org/10.1038/s41586-025-09945-5

Received: 21 January 2025

Accepted: 20 November 2025

Published online: 14 January 2026

Check for updates

Batsheva Rozman[1,8]✉, Karin Broennimann[2,8], K. Shanmugha Rajan[3,8], Aharon Nachshon[1], Chiranjeet Saha[3], Tamar Arazi[1], Vishnu Mohan[4], Tamar Geiger[4], Clayton J. Wollner[5], Justin M. Richner[5], Eric Westhof[6,7], Ada Yonath[3], Anat Bashan[3] & Noam Stern-Ginossar[1]✉

The considerable success of mRNA vaccines against SARS-CoV-2 has underscored the potential of synthetic mRNA as a transformative biomedical technology[1]. A critical feature of this approach is the incorporation of the modified nucleoside N^1-methylpseudouridine ($m^1\Psi$), which enhances antigen expression while reducing immunogenicity[2–5]. However, a comprehensive understanding of how $m^1\Psi$ influences translation remains incomplete. Here we use ribosome profiling at the subcodon resolution to show that $m^1\Psi$ increases ribosome density on synthetic mRNAs, leading to higher protein production independent of innate immune activation or eIF2α phosphorylation. We find that $m^1\Psi$ directly slows ribosome movement in defined sequence contexts while simultaneously promoting translation initiation. Structural studies using cryo-electron microscopy reveal that $m^1\Psi$ alters interactions with in the ribosomal decoding centre, providing a mechanistic basis for slowed elongation. Furthermore, by introducing synonymous recoding that disrupts the modification-mediated changes in elongation, we show that the $m^1\Psi$-dependent enhancement of protein output is modulated by codon composition, and that $m^1\Psi$ impact is strongest in mRNAs containing non-optimal codons with uridines at the wobble position. Together, these findings demonstrate that $m^1\Psi$ directly modulates translation dynamics, thereby increasing protein yield from synthetic mRNAs in specific sequence contexts.

A key feature of therapeutic in vitro-transcribed (IVT) mRNAs is the incorporation of modified nucleosides, which have been shown to reduce innate immune recognition and enhance mRNA stability, both advantageous traits for mRNA-based therapies[2,3,5,6]. Despite their extensive use[7], there is limited understanding of how these ribonucleotide modifications, such as pseudouridine (Ψ) and $m^1\Psi$, directly influence mRNA decoding by the ribosome. Recent studies indicate that $m^1\Psi$ can induce +1 ribosomal frameshifting[8], and both Ψ and $m^1\Psi$ were shown to influence protein synthesis rates in vitro, suggesting a direct effect on translation[9–12]. However, the extent of these phenomena in mammalian cells and the specific sequence contexts in which they occur remain unclear. Understanding these processes is critical for deepening our knowledge of translation dynamics from modified IVT mRNA and for the optimized design and evaluation of next-generation mRNA therapeutics.

Modified mRNA has increased ribosome load

To examine whether and how Ψ and $m^1\Psi$ influence translation inside cells, we synthesized IVT mRNAs encoding the SARS-CoV-2 spike protein, incorporating either UTP, Ψ or $m^1\Psi$ at each uridine position. After confirming RNA integrity and removing residual double-stranded RNA (dsRNA)[13] (Extended Data Fig. 1a,b), we transfected the purified mRNAs into HEK293T cells. At 24 h after transfection, cells were collected for ribosome profiling, RNA sequencing (RNA-seq) (Fig. 1a) and western blot analysis (Fig. 1b and Extended Data Fig. 1c) with two independent biological replicates. The mRNA and ribosome footprint measurements were reproducible across all samples (Extended Data Fig. 1d). The footprint read-length distribution was similar between samples, peaking at 29 nucleotides, in alignment with previous ribosome footprint analyses[14] (Extended Data Fig. 1e). Metagene analysis of the P-site position of reads revealed the expected profiles for ribosome-protected footprints with a three-base periodicity (Extended Data Fig. 1f). Given that ribosome profiling depends on RNase digestion and Ψ or $m^1\Psi$ was suggested to resist nuclease cleavage[15,16], we confirmed that these modifications did not affect footprint mapping. Read-length distributions of IVT and endogenous mRNAs were indistinguishable across all samples (Extended Data Fig. 1g). Moreover, the proportion of reads with uridines at the 3′ and 5′ ends showed no differences between modified and unmodified mRNA (Extended Data Fig. 1h), indicating Ψ

[1]Department of Molecular Genetics, Weizmann Institute of Science, Rehovot, Israel. [2]Department of Immunology and Regenerative Biology, Weizmann Institute of Science, Rehovot, Israel. [3]Department of Chemical and Structural Biology, The Weizmann Institute of Science, Rehovot, Israel. [4]Department of Molecular Cell Biology, Weizmann Institute of Science, Rehovot, Israel. [5]Department of Microbiology and Immunology, College of Medicine, University of Illinois Chicago, Chicago, IL, USA. [6]Architecture et Réactivité de l'ARN, Université de Strasbourg, Institut de biologie moléculaire et cellulaire du CNRS, Strasbourg, France. [7]Engineering Research Center of Clinical Functional Materials and Diagnosis & Treatment. Devices of Zhejiang Province, Wenzhou Institute, University of Chinese Academy of Sciences, Wenzhou, China. [8]These authors contributed equally: Batsheva Rozman, Karin Broennimann, K. Shanmugha Rajan. ✉e-mail: batsheva.frankelrozman@weizmann.ac.il; noam.stern-ginossar@weizmann.ac.il

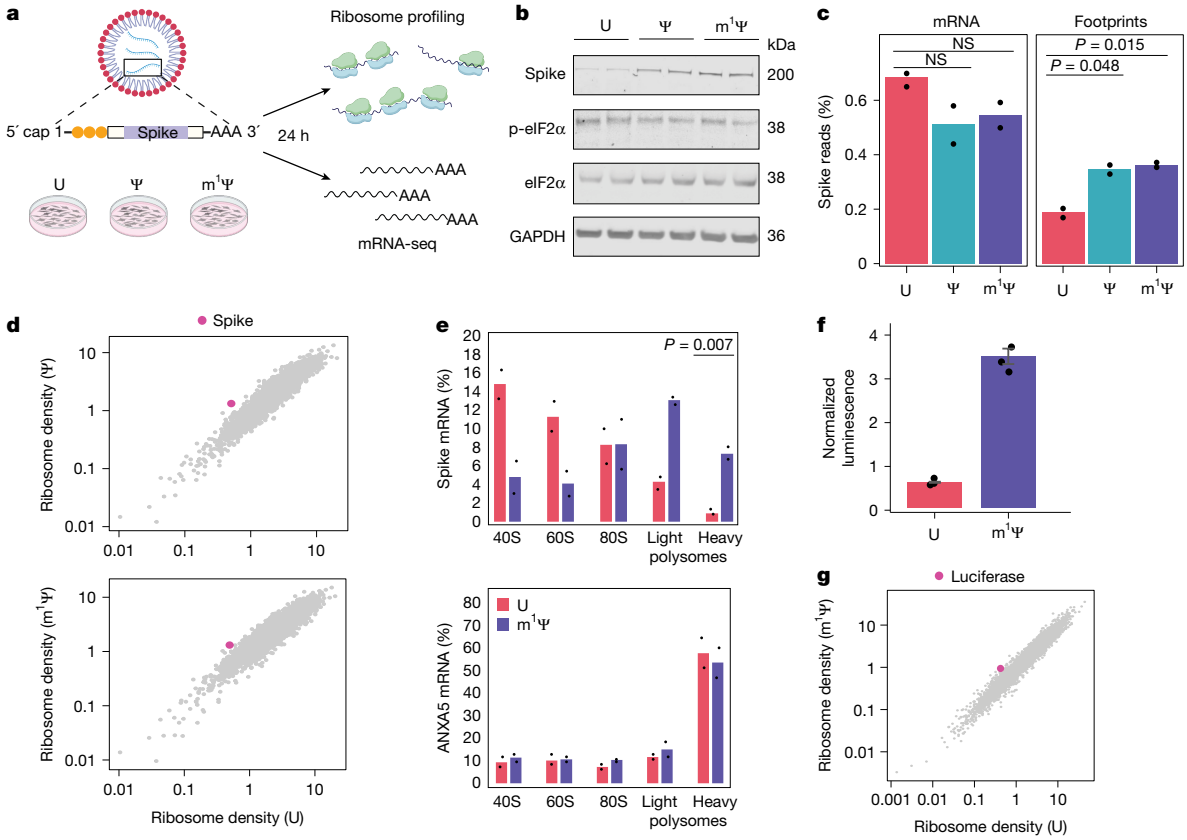

Fig. 1 | Modified transcripts exhibit higher ribosome occupancy. a, The experimental setup. The diagram was created using BioRender. **b**, Western blot analysis of spike protein expression and eIF2α phosphorylation levels of cells transfected with IVT mRNA containing UTP, Ψ or m^{1}Ψ in two biological replicates. **c**, The percentage of reads on spike mRNA from RNA-seq and ribosome profiling samples. Data are mean and points show the values for each replicate. *P* values were calculated using two-sided Student's *t*-tests. **d**, Ribosome densities, calculated as the ratio of footprints to mRNA levels, for human genes (grey) and spike mRNA (pink). Cells transfected with UTP were compared with Ψ-modified mRNA (top) or m^{1}Ψ-modified mRNA (bottom). **e**, The relative distribution of spike mRNA (top) and *ANXA5*, an endogenous transcript (bottom) across polysome fractions. RNA from gradient fractions (presented in Extended Data Fig. 1i) was extracted and quantified using quantitative PCR with reverse transcription (RT–qPCR). Data are the mean of two independent biological replicates and the points show individual values. *P* values were calculated using two-sided Student's *t*-tests. **f**, Firefly luciferase luminescence levels (normalized to *Renilla* luciferase) from cells transfected with luciferase mRNA containing UTP or m^{1}Ψ. Data are mean ± s.d. of three biological replicates. **g**, Ribosome densities, calculated as the ratio of ribosome footprints to mRNA levels, for human genes (grey) and luciferase mRNA (pink).

and m^{1}Ψ do not interfere with library preparation or codon-resolution mapping accuracy.

Consistent with previous reports[3,4], Ψ- and m^{1}Ψ-containing mRNAs produced 3.2- and 3.7-fold more spike protein (Fig. 1b and Extended Data Fig. 1c), indicating that modified mRNAs were translated more efficiently than non-modified mRNA. Analysis of RNA-seq data revealed a slight reduction in the modified spike mRNA levels compared with the non-modified spike, but these differences were not significant (Fig. 1c). Nevertheless, in the ribosome profiling data, a significant increase was observed in the proportion of footprints originating from spike mRNA in the Ψ- and m^{1}Ψ-modified samples (Fig. 1c). Correspondingly, we observed a significant increase in ribosome densities (calculated as the number of footprints divided by the number of RNA-seq reads) on Ψ- and m^{1}Ψ-modified spike mRNAs compared with the UTP spike mRNA, with ribosome densities increasing 2.8-fold and 2.6-fold, respectively (Fig. 1d). To further validate this specific increase in ribosome load of modified mRNA, we performed polysome profiling on cells transfected with UTP or m^{1}Ψ-modified spike mRNA (Extended Data Fig. 1i) and quantified the distribution of spike mRNA across the polysome gradient. We observed a clear shift of the m^{1}Ψ-modified spike mRNA into heavier polysome fractions compared with the unmodified mRNA (Fig. 1e (top)). By contrast, the endogenous *ANXA5* mRNA showed no difference between UTP- and m^{1}Ψ-transfected cells (Fig. 1e (bottom)), confirming that m^{1}Ψ modification selectively promotes increased ribosome loading on modified IVT mRNAs.

We next tested whether the increase in ribosome load could be reproduced using another modified mRNA. We selected a firefly luciferase reporter, which allows sensitive measurement of protein expression, and focused on m^{1}Ψ modification. Firefly luciferase IVT mRNA containing UTP or m^{1}Ψ was transfected into HEK293T cells, and analysed by luciferase assay, RNA-seq and ribosome profiling. Incorporation of m^{1}Ψ led to a 4.4-fold increase in luciferase signal compared to UTP mRNA (Fig. 1f) and, consistent with our spike mRNA results, to higher ribosome density on m^{1}Ψ-modified luciferase mRNA (Fig. 1g). Polysome profiling further revealed a shift of the m^{1}Ψ-modified luciferase mRNA toward polysome fractions (Extended Data Fig. 1j,k), an effect not observed for endogenous mRNA (Extended Data Fig. 1l).

Notably, the enhanced ribosome load on modified transcripts cannot be attributed to global translation changes such as the one mediated by PKR (encoded by *EIF2AK2*) activation and eIF2α phosphorylation[5,9], as ribosome profiling measures relative rather than absolute ribosome occupancy. The observed increase in ribosome load specifically on modified mRNAs therefore reflects a direct and modification-specific change in translation. Consistently, eIF2α phosphorylation levels showed only minimal differences between modified and unmodified mRNAs (Fig. 1b and Extended Data Fig. 1c), and global polysome profiles were unchanged (Extended Data Fig. 1i,j). Analysis of *ATF4*, *CHOP*

and other eIF2α-responsive mRNAs[17] or interferon-stimulated genes in the ribosome profiling and mRNA expression data revealed no significant changes in cells transfected with Ψ- or m^{1}Ψ-modified mRNAs (Extended Data Fig. 1m), arguing against PKR activation as the main driver of increased ribosome density and protein expression.

Ψ has been shown to weaken stop codon recognition and promote ribosomal readthrough[18–20], but whether m^{1}Ψ exerts a similar effect remains unclear. To examine this, we measured footprints in the 3′ untranslated region (UTR) of modified versus unmodified transcripts. The spike mRNA, which contains four consecutive stop codons, provides little opportunity for readthrough; accordingly, no differences in 3′ UTR ribosome occupancy were detected. By contrast, luciferase mRNA, which contains a single UAA stop codon, exhibited markedly increased 3′-UTR ribosome occupancy in m^{1}Ψ-modified mRNA (Extended Data Fig. 1n). Moreover, both modified mRNAs showed a trend toward shorter ribosome dwell times at the stop codon, suggesting reduced termination fidelity (Extended Data Fig. 1o).

Ψ and m^{1}Ψ slow elongating ribosomes

Our analysis revealed higher ribosome densities specifically on Ψ- and m^{1}Ψ-modified mRNA. An increase in ribosome number may arise from elevated translation initiation, leading to more ribosomes engaging with the mRNA, or from slower ribosome translocation across the coding sequence (CDS), as previously reported[9,10]. To test whether Ψ or m^{1}Ψ directly influence elongation dynamics, we analysed ribosome footprint distributions along spike and luciferase mRNAs. We observed numerous footprint peaks unique to the Ψ- and m^{1}Ψ-modified mRNAs, indicating specific changes in the elongation rate (Fig. 2a and Extended Data Fig. 2a). Principal component analysis of footprint densities at each codon also showed a clear separation between Ψ- or m^{1}Ψ-modified and unmodified mRNAs, suggesting that these modifications induce similar codon-specific alterations in translation kinetics (Extended Data Fig. 2b,c).

During elongation, the ribosome decodes mRNA one codon at a time, cycling tRNAs through the A, P and E sites. We focused on A-site codons, where decoding occurs, and calculated the relative ribosome footprint densities for each codon along the spike and luciferase CDS for Ψ- and m^{1}Ψ-modified versus unmodified mRNA. Grouping codons by their uridine content revealed a significant increase in ribosome dwell time on modified transcripts specifically at A-site codons containing uridine, with the effect strengthening as the number of uridines in the codon increased (Fig. 2b and Extended Data Fig. 2d).

To refine our analysis, we stratified codons with a single uridine based on its position within the codon—first, middle or third. Codons with a middle-position uridine showed a significant ribosome dwell time increase in both Ψ- and m^{1}Ψ-modified mRNAs, while those with a uridine in the first or third positions did not (Fig. 2c and Extended Data Fig. 2e). Similarly, codons containing two uridines exhibited the strongest increase when one of the uridines occupied the middle position (Extended Data Fig. 2f,g). No significant changes in ribosome dwell times were observed for uridine-containing codons in the endogenous *Actb* mRNA, illustrating that the effect is specific to the modified IVT mRNA (Extended Data Fig. 2h).

We next examined P-site codons, where peptide bond formation occurs, and revealed a distinct signature: Ψ- and m^{1}Ψ-modified mRNAs showed increased dwell times when the modified uridine was in the third codon position (Fig. 2d and Extended Data Fig. 2i). Assessing a potential additive effect, we found the strongest increase in dwell time when a modified uridine occupied the middle A-site position and the third P-site position (NUN, NNU codon pairs) (Fig. 2e and Extended Data Fig. 2j).

To further systematically test sequence-context effects, we performed differential expression analysis of ribosome footprint densities at each codon using DESeq2. Codons with over twofold change and $P < 0.01$ were classified as significantly affected by the modification. Fisher's exact test on A-, P- and E-site codons at these sites revealed strong enrichment for NUN and NNU codons in the A and P sites (Fig. 2f and Extended Data Fig. 2k).

Finally, to directly assess whether m^{1}Ψ affects elongation kinetics, we transfected cells with luciferase mRNA containing UTP or m^{1}Ψ and performed ribosome run-off experiments[21]. Translation initiation was blocked with harringtonine, and ribosome profiling at multiple timepoints thereafter captured a dynamic view of elongation progression. Metagene analysis of cellular transcripts showed the expected 5′- to 3′-end ribosome depletion, with average elongation rates of 4.38 and 4.98 amino acids per second for cells transfected with UTP and m^{1}Ψ IVT mRNAs, respectively (Extended Data Fig. 2l), consistent with previous reports[21]. While run-off kinetics for endogenous transcripts showed comparable values, ribosomes advanced significantly more slowly along the m^{1}Ψ-modified luciferase mRNA compared to its unmodified counterpart (Fig. 2g and Extended Data Fig. 2m), providing direct evidence that m^{1}Ψ incorporation reduces ribosome elongation speed.

m^{1}Ψ modifies decoding centre geometry

To gain mechanistic insights into how m^{1}Ψ slows translation at NNU,NUN codon pairs, we determined high-resolution cryo-electron microscopy (cryo-EM) structures of human 80S ribosomes programmed with synthetic RNAs containing either UTP or m^{1}Ψ in the A- and P-site codons. Ribosomes were trapped in the post-decoding, pre-translocation (classical-PRE) state[22] using preprogrammed mRNAs, human tRNAs and hygromycin B stabilization. We obtained maps at a resolution of around 2.4 Å for both modified (m^{1}Ψ–PRE) and unmodified (uridine–PRE) complexes (Extended Data Table 1 and Extended Data Fig. 3a,b). The high-resolution EM maps enabled complete modelling of all ribosomal proteins, rRNAs and known modifications, with clear density for the P-site tRNA^{Arg}[23] (Extended Data Fig. 4a), consistent with the human 80S reference structure (Protein Data Bank (PDB): 8GLP)[24], and the codon-anticodon region closely resembled the yeast-PRE reference structure (PDB: 8CDL)[25] (Extended Data Fig. 4b–f).

Closer inspection of the decoding centre showed the ribose of m^{1}Ψ(+3), located at the A/P kink (Fig. 3a), adopts a C2′-*endo* sugar pucker (Fig. 3b), as observed in recent functional ribosome complexes[26], including in our uridine–PRE complex (Extended Data Fig. 4g). By contrast, both m^{1}Ψ(+5) and U(+5) retain the typical C3′-*endo* conformation (Fig. 3b). As pseudouridines and their derivatives favour C3′-*endo* conformation[27,28], the enforced shift of m^{1}Ψ(+3) to C2′-*endo* after movement from A to P site is probably energetically unfavourable, potentially slowing elongation.

Notably, in the m^{1}Ψ–PRE complex, we observed *syn* conformations of the purine bases at G(+2) in the P-site mRNA and in the A35 of the A-site tRNA (Extended Data Fig. 4h,i), enabling Hoogsteen base-pairing, an alternative hydrogen-bonding mode distinct from classical Watson–Crick interactions (Fig. 3c). In the uridine–PRE complex, the G(+2) and A35 nucleotides are predominantly in the *anti* conformation (Extended Data Fig. 4h). The unusual apparent preference for *syn* over the typical *anti* conformation[29] may reflect enhanced stacking between adjacent m^{1}Ψ residues and reduced steric clash, stabilizing an alternative local geometry. Similar *syn* conformations have been observed in ribosomes containing Pseudouridines at stop codons[19], suggesting that m^{1}Ψ can locally remodel the decoding centre to permit non-canonical base pairing that may hinder translocation. However, we cannot exclude that the use of short linear RNA allows greater rotational freedom, potentially facilitating these conformations.

Together, these features, the enforced C2′-*endo* sugar pucker at the third position of the P-site and Hoogsteen base pairing driven by *syn* conformations in nearby purines, define an m^{1}Ψ-specific structural signature. This altered geometry provides a potential mechanistic basis for the increased ribosome dwell times observed on m^{1}Ψ-modified transcripts.

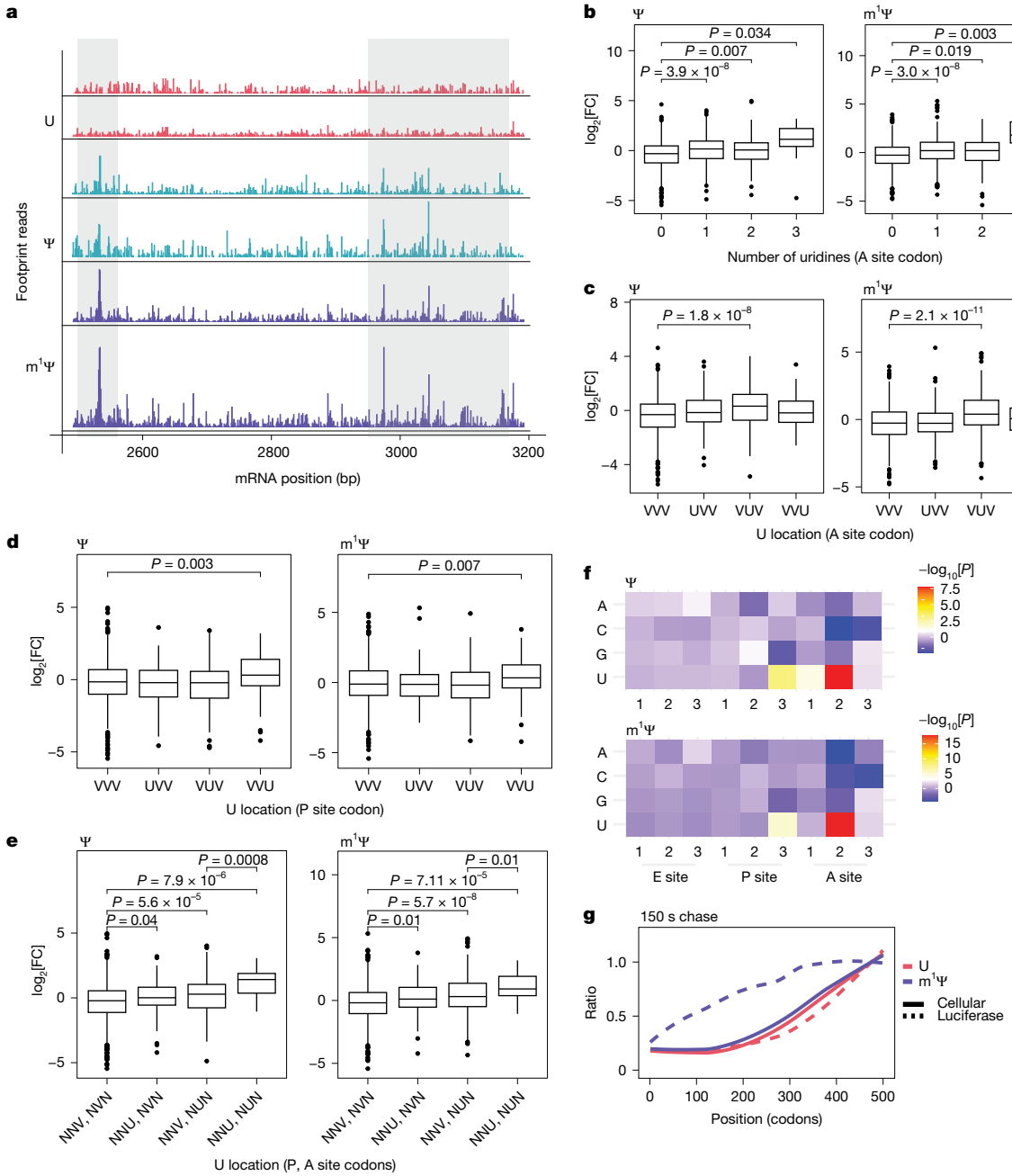

Fig. 2 | Modified nucleotides slow translation elongation in a specific sequence context. a, Snapshot of ribosome footprint profiles along a segment of the spike mRNA with UTP (red), Ψ (light blue) or m^{1}Ψ (blue). The bars show the read coverage at every nucleotide. The grey squares highlight differences in profiles. Each line represents a profile of an independent biological duplicate **b**–**e**, The $\log_2$-transformed fold change in relative ribosome densities of modified mRNA compared with non-modified mRNA in codons binned based on the number of uridines in the A site (**b**), by the location of uridine in the A site (**c**), by the location of uridine in the P site codon (**d**) and by location of uridine in the A-site and P-site codons (**e**). V represents non-uridine bases. *P* values were calculated using two-sided standard Student's *t*-tests. The box plots show the median (centre line), interquartile range (IQR; box limits) and the whiskers extend to 1.5 × IQR; the points indicate outliers. All datapoints represent the mean of two independent biological replicates of the ribosome profiling. **f**, Heatmaps showing the $-\log_{10}$-transformed *P* values from nucleotide enrichment tests at each position (E,P,A site) for positions with ribosome densities that differ significantly between the modified conditions and UTP. Results are shown for Ψ (top) or m1Ψ (bottom). Positive values indicate enrichment whereas negative values indicate depletion. **g**, Metagene analysis of ribosome run-off at 150 s after Harringtonine addition for cellular (solid line) and luciferase (dashed line) mRNAs from cells transfected with UTP (red) or m^{1}Ψ (blue) luciferase mRNAs. Smoothed ribosome densities are presented as the ratios relative to the 0 timepoint.

Enhanced initiation on modified mRNA

Slower elongation may contribute to the increased ribosome load on Ψ- and m^{1}Ψ-modified transcripts; however, this alone cannot explain the higher spike and luciferase protein levels. Enhanced protein synthesis typically reflects increased translation initiation—the rate-limiting step of translation[30,31]. Cellular sensing of foreign RNA can inhibit initiation through PKR-mediated eIF2α phosphorylation, but our analyses showed no evidence of this mechanism.

Moreover, enhanced luciferase expression from m^{1}Ψ-modified relative to unmodified mRNAs was observed both in *EIF2AK2*-knockout (KO) HEK293T cells[32] (Fig. 4a and Extended Data Fig. 5a,b) and

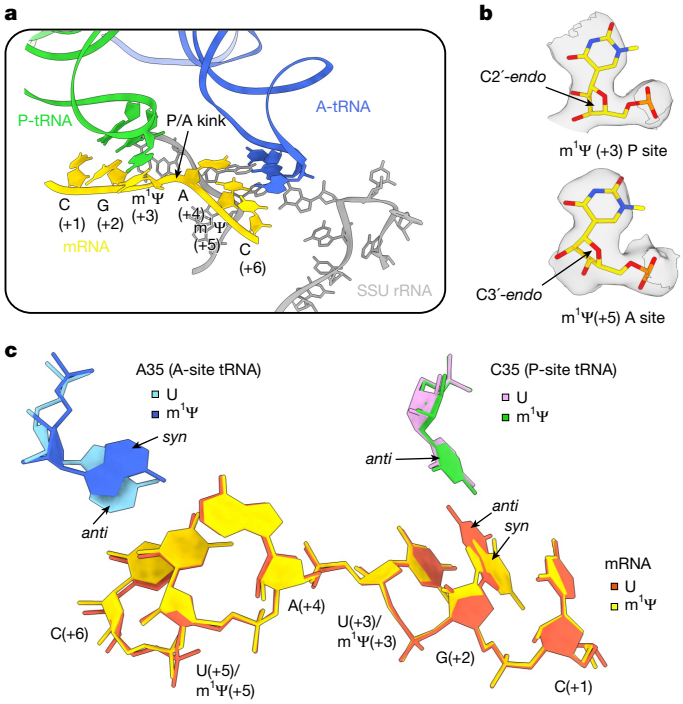

Fig. 3 | Atomic snapshot of codon–anticodon geometry in the m^{1}Ψ–PRE ribosome complex. a, Magnified image of the nucleotides near the P/A kink, shown with respect to the A-site and P-site anticodons in the tRNAs. The mRNA nucleotides are numbered from +1 to +6. The mRNA, A-site tRNA, P-site tRNA and SSU rRNA are shown as gold, blue, green and grey ribbons, respectively. **b**, Sugar puckers of the two m^{1}Ψ nucleotides. The cryo-EM density of the m^{1}Ψ in the +3 and +5 positions is shown. The sharpened experimental EM map is depicted as a grey surface ($\sigma = 2.7$). **c**, Structural comparison of nucleotide geometry in the decoding centre of uridine–PRE and m^{1}Ψ–PRE complexes. Nucleotides are coloured as in **a** for the m^{1}Ψ–PRE complex. mRNA, A-site tRNA and P-site tRNAs in the uridine–PRE complex are highlighted in orange, sky-blue and pink, respectively.

after treatment with ISRIB—a small molecule that blocks the downstream effects of eIF2α phosphorylation[33] (Fig. 4b and Extended Data Fig. 5c). To rule out potential confounding effects of residual dsRNA, all of the following experiments were conducted in *EIF2AK2*-KO cells.

We examined other potential contributors to increased protein levels, including mRNA stability[34], capping efficiency[35], subcellular distribution[36,37] and protein stability. Comparative analyses of mRNA decay, capping strategies, cytosolic versus membrane-associated RNA fractions and luciferase protein half-lives revealed no significant differences between modified and unmodified transcripts (Extended Data Fig. 5d–i). These results suggest that increased translation initiation, rather than innate immune sensing, altered RNA metabolism or protein turnover, underlies the increased protein expression from modified mRNAs.

In an attempt to separate effects on elongation from those on initiation, we reanalysed ribosome densities along spike and luciferase mRNAs after excluding positions where the P- or A-site codons contained uridines, thereby potentially reducing most site-specific elongation-related effects. Even at these uridine-free sites, Ψ- and m^{1}Ψ-modified transcripts showed significantly higher ribosome occupancy (2.6- and 2.4-fold, respectively; Extended Data Fig. 5j), consistent with an overall increase in translation initiation. A similar trend was observed for luciferase mRNA (1.4-fold increase), indicating that the elevated ribosome load is probably not solely attributed to slowed elongation.

As translation initiation is influenced by the 5′-UTR sequence, which is also modified in our IVT mRNAs, we tested whether modified uridines in the 5′ UTR explain the modification-dependent increase in protein levels, as has been reported for some sequences[35]. We synthesized luciferase mRNA with UTP or m^{1}Ψ with either wild-type (WT) 5′ UTRs or uridine-depleted 5′ UTRs. After transfection into cells, we observed increased luciferase activity from m^{1}Ψ-modified mRNA, regardless of the 5′-UTR sequence (Fig. 4c), suggesting that m^{1}Ψ incorporation along the CDS may impact translation initiation.

To assess translation initiation, we measured recruitment of the cap-binding protein eIF4E. eIF4E binding to the mRNA cap is a sensitive indicator of initiation efficiency, as its affinity is enhanced by eIF4G and PABP interactions that stabilize cap binding and promote ribosome loading[38–40]. eIF4E RNA immunoprecipitation (IP) from *EIF2AK2*-KO cells transfected with UTP or m^{1}Ψ-modified luciferase mRNAs lacking uridines in the 5′ UTR revealed significantly greater binding of m^{1}Ψ-modified mRNA to eIF4E, whereas endogenous mRNAs showed no difference (Fig. 4d–f and Extended Data Fig. 5k). These results suggest that the translation of m^{1}Ψ-modified mRNA is enhanced, and increased recruitment of the translation initiation machinery depends on uridines in the CDS.

Functional impact of slowed elongation

To investigate whether changes in elongation contribute to the observed effects on protein output and to broadly explore the functional consequences of Ψ or m^{1}Ψ-induced slowing of elongation, we considered three non-exclusive scenarios: (1) changes in elongation rate affect translational fidelity; (2) slowed elongation increases ribosomal frameshifting, as recently reported[8]; and (3) changes in elongation impact protein yield from modified mRNA.

To examine whether Ψ or m^{1}Ψ impact the accuracy of ribosome decoding, UTP, Ψ or m^{1}Ψ spike encoding mRNAs were transfected into cells and 24 h after transfection cells were lysed and the spike protein was pulled-down using a monoclonal antibody (Extended Data Fig. 6a). The eluted protein was analysed using mass spectrometry (MS) for misincorporation of amino acids in each sample. We did not observe significant increase in the miscoding frequency for spike protein expressed from modified mRNA compared with non-modified mRNA, indicating that, in agreement with previous findings[41], modification-dependent changes in translation elongation do not seem to lead to substantial changes in translation fidelity (Extended Data Fig. 6b).

Changes in translation elongation can disrupt reading frame maintenance, and a recent study reported that m^{1}Ψ incorporation induces +1 ribosomal frameshifting[8]. To evaluate and quantify potential m^{1}Ψ-induced frameshifting in our ribosome profiling data, we analysed ribosome footprint distributions across the three reading frames in modified and non-modified spike mRNA. No significant differences were observed in the +1-frame fraction (Extended Data Fig. 6c), indicating that m^{1}Ψ does not cause major +1 frameshifting. A slight increase in −1-frame reads was detected in Ψ-modified mRNA, but these were comparable to distributions in human transcripts, suggesting minor technical variation during library preparation.

Frameshifting often occurs at 'slippery sites', where codons in the 0 and +1 frames can be read by the same tRNA. We therefore calculated frame distributions downstream of each slippery site and up to the first +1-frame stop codon, comparing observed values to randomized baselines and computing *Z*-scores to measure deviations. While some individual slippery sites exhibited significant frame deviations, there were no significant differences between slippery sites containing or lacking uridines (Extended Data Fig. 6d), indicating these could reflect noise rather than m^{1}Ψ-induced frameshifting.

To assess our detection sensitivity, we simulated varying levels of frameshifting and found that our data could reliably detect moderate events (≥5%) with no evidence of modification-dependent

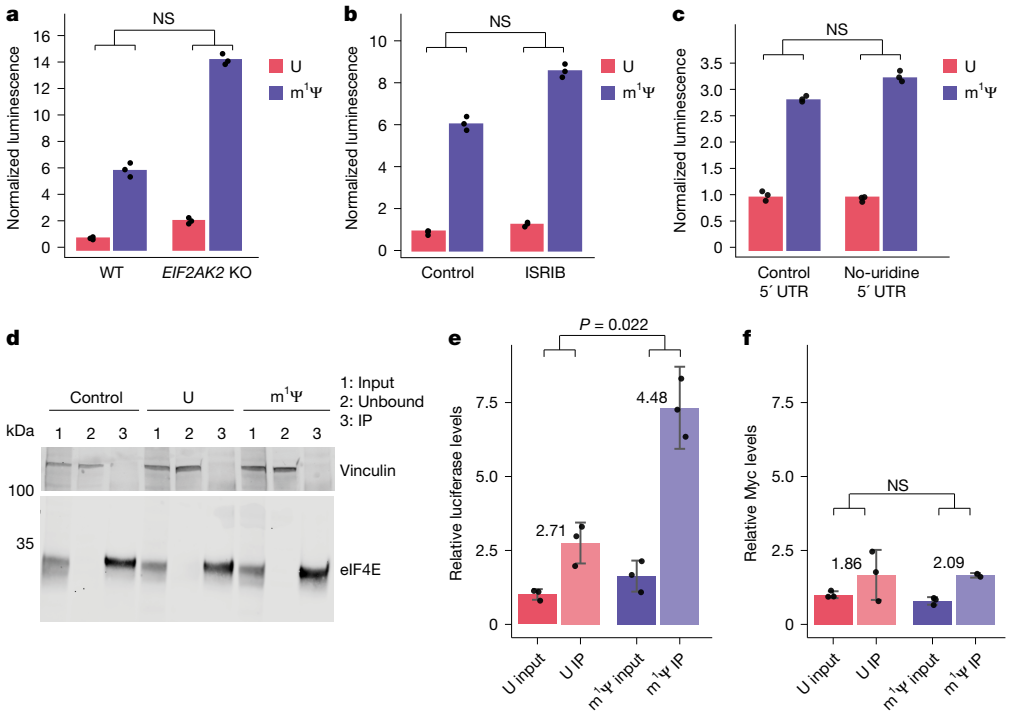

Fig. 4 | Enhanced translation initiation underlies increased expression from m^{1}Ψ-modified mRNAs. a–**c**, The mean ± s.d. luciferase expression from three biological replicates. Cells were transfected with luciferase IVT mRNA containing UTP or m^{1}Ψ. **a**, WT versus *EIF2AK2*-KO cells. **b**, Cells were untreated (control) or treated with ISRIB. **c**, Cells were transfected with luciferase carrying a WT 5′-UTR (control) or a 5′ UTR lacking uridines (no-uridine). Statistical significance was calculated using linear regression. **d**, Western blot analysis of the levels of eIF4E after IP with anti-eIF4E antibodies. The lanes: 1, input samples; 2, unbound fraction; 3, bound IP fraction for non-transfected control cells, cells transfected with UTP or m^{1}Ψ-modified luciferase mRNAs are shown. Vinculin is presented as the loading control. **e**,**f**, Luciferase (**e**) and *Myc* (endogenous control) mRNA levels (**f**) in input and eIF4E-IP samples from cells transfected with UTP- or m^{1}Ψ-modified luciferase mRNAs, measured using RT–qPCR. Data are mean ± s.d. of three biological replicates. Statistical significance was calculated using linear regression. The fold change between the input and IP for each sample is indicated on the graph.

frameshifting at this threshold (Extended Data Fig. 6d). Moreover, we investigated whether +1 frameshifting occurs at codons associated with slowed translation elongation. Analysis of codons showing the strongest m^{1}Ψ:UTP differences in ribosome densities revealed no significant enrichment for +1 frameshifting events (Extended Data Fig. 6e). Together, these results indicate that any modification-dependent frameshifting occurring in cells is probably low and below the detection limit of our measurements.

m^{1}Ψ impact depends on coding context

To determine whether m^{1}Ψ-driven elongation changes influence protein output, we exploited wobble-position synonymous mutations that alter the sequence context without changing the protein sequence. We designed a spike mRNA variant (spike-minU) with reduced uridine content (reduced from 20% to 14%) and nearly all NNU,NUN codon pairs removed (the sequences are provided in Supplementary Table 1). Synthesized with either UTP or m^{1}Ψ and transfected into cells, spike-minU showed a smaller protein expression difference between UTP and m^{1}Ψ compared with the original spike, with no major changes in mRNA abundance (Fig. 5a and Extended Data Fig. 7a,b). To enhance sensitivity, we generated luciferase variants: MinU (fewer wobble uridines) and MaxU (more wobble uridines) (sequences are provided in Supplementary Table 1). Compared with the WT, the UTP- m^{1}Ψ expression difference was smaller for MinU but larger for MaxU (Fig. 5b), without major effects on mRNA abundance (Extended Data Fig. 7c).

We also analysed GFP, which, due to extensive codon optimization, contains only four wobble uridines and two NNU,NUN instances (sequences are provided in Supplementary Table 1). Accordingly, GFP showed minimal differences between UTP and m^{1}Ψ-containing mRNAs (Fig. 5c and Extended Data Fig. 7d,e). Recoding GFP to increase the number of wobble uridines (sequences are provided in Supplementary Table 1) restored the modification-dependent enhancement: m^{1}Ψ-recoded GFP produced higher protein levels than its UTP counterpart, without major changes in mRNA abundance (Fig. 5c and Extended Data Fig. 7f).

Ribosome profiling of cells transfected with WT or MinU luciferase mRNAs carrying a uridine-depleted 5′ UTR with either UTP or m^{1}Ψ-modified mRNA revealed the expected signal in the WT sample: increased dwell time at NNU codons in the P site and NUN codons in the A site (Extended Data Fig. 7g). Codon positions showing significantly elevated ribosome dwell time (DESeq2 analysis in which modified codons showed FC > 2 and $P < 0.01$) in m^{1}Ψ-modified WT luciferase (relative to the UTP) displayed a reduced signal at the same codon positions in the MinU mRNA, indicating that m^{1}Ψ at the P-site wobble position indeed alters elongation dynamics (Fig. 5d). Furthermore, to assess a potential link between CDS composition and modification-driven changes in initiation, we analysed ribosome densities on 6-mers lacking uridines. As anticipated, m^{1}Ψ-modified WT luciferase exhibited a 2.7-fold increase in ribosome load relative to the UTP control, whereas the m^{1}Ψ-modified MinU mRNA showed only a minimal increase (Extended Data Fig. 7h). These findings suggest that changes in m^{1}Ψ abundance along the CDS modulate both translation elongation and initiation, shaping the protein output.

By altering the CDSs of spike, luciferase and GFP we were able to modulate the extent of m^{1}Ψ-dependent effect on protein expression. To gain deeper insight into the sequence features dictating the magnitude of m^{1}Ψ's impact on translation, we generated a library of 305 luciferase-encoding barcoded mRNAs containing synonymous mutations that systematically varied in overall uridine content and

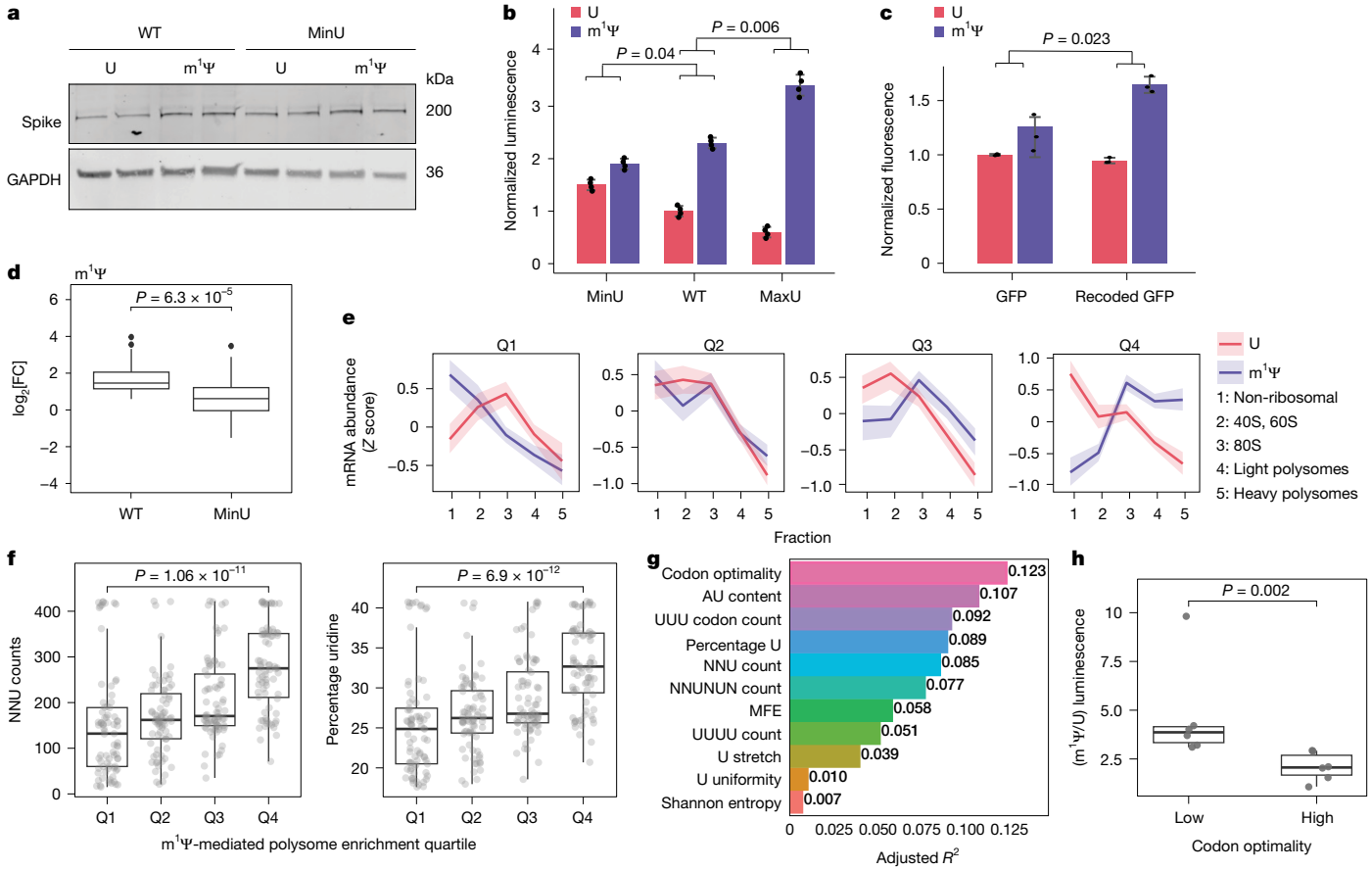

Fig. 5 | m^{1}Ψ impact is strongest in mRNAs with non-optimal codons. **a**, Western blot analysis of spike protein levels (in duplicates) in cells transfected with IVT mRNAs WT spike (used throughout this study) or MinU spike (reduced uridines) with UTP or m^{1}Ψ. GAPDH was used as the loading control. Quantification is shown in Extended Data Fig. 7a. **b**, Firefly luciferase activity (normalized to *Renilla*) for three luciferase mRNAs: MinU (reduced wobble-position U), WT (used throughout this study) and MaxU (increased wobble-position U). Data are mean ± s.d. of three biological replicates. **c**, The GFP mean fluorescence intensity, measured using fluorescence-activated cell sorting (FACS) analysis of cells transfected with GFP and recoded-GFP (increased wobble-position U) IVT mRNAs. Data are mean ± s.d. of three biological replicates. For **b** and **c**, *P* values were calculated using linear regression. **d**, The $\log_2$-transformed fold-change in ribosome density (m^{1}Ψ-modified versus unmodified) in WT and MinU for codons showing over a two-fold change and $P < 0.01$ in the WT. *P* values were calculated using two-sided Student's *t*-tests. The box plots show the median (centre line), interquartile range (IQR; box limits), and the whiskers extend to 1.5 × IQR; the points indicate outliers. All datapoints represent the mean of two independent biological replicates of ribosome profiling. **e**, mRNA abundance (*Z* score) across the five fractions of the polysome profile (1, non-ribosomal; 2, 40S and 60S; 3, 80S; 4, light polysomes; 5, heavy polysomes). The curves represent the mean values of mRNAs grouped by m^{1}Ψ-mediated polysome enrichment score, with UTP (red) and m^{1}Ψ (blue). The shaded regions denote the 95% confidence intervals. **f**, NNU codon frequency (left) and overall uridine content (right) across m^{1}Ψ-mediated polysome enrichment quartiles. The points represent individual sequences averaged across three independent replicates for each sample. *P* values were calculated using two-sided Student's *t*-tests. The box plots show the median (centre line), interquartile range (IQR; box limits) and the whiskers extend to 1.5 × IQR; the points indicate outliers. **g**, The adjusted R^2 values for individual sequence features, reflecting their contribution to variance in m^{1}Ψ-mediated polysome enrichment score **h**, m^{1}Ψ/UTP firefly luciferase activity ratios (normalized to *Renilla*) for six representative high or low codon-optimality sequences. $n = 3$ biologically independent replicates. Statistical significance was assessed using two-sided Wilcoxon matched-pairs tests. The box plots show the median (centre line) and 25th and 75th percentiles (box limits), and the points show the individual median values for each sequence.

frequency of NNU,NUN codon pairs (Supplementary Table 1 (fluc_ library)). To specifically assess CDS effects, all sequence variants shared the first 39 nucleotides after the start codon and the last 39 nucleotides before the stop codon. The library was transcribed in vitro in a pooled format using either UTP or m^{1}Ψ and transfected into *EIF2AK2*-KO cells. Twelve hours after transfection, we performed polysome profiling and collected mRNAs and sequenced the library from both whole-cell lysates and fractions spanning the polysome profile (Extended Data Fig. 8a). For a subset of sequences, we designed two unique barcodes per sequence and confirmed that their distribution across polysome fractions was consistent, ensuring that observed distribution patterns were not due to barcode-specific effects (Extended Data Fig. 8b). Biological triplicates showed strong reproducibility, and principal component analysis showed separation between UTP and m^{1}Ψ samples, demonstrating a specific effect of m^{1}Ψ on translation (Extended Data Fig. 8c,d).

For each sequence, we computed a polysome enrichment score as the ratio of m^{1}Ψ:UTP reads in polysome fractions relative to the ratio in the non-ribosomal fraction (Extended Data Fig. 8e). Sequences were divided, based on this score, into four quartiles (Q1–Q4), representing increasing degrees of m^{1}Ψ-dependent polysome enrichment (Fig. 5e). An analysis of CDS features across these quartiles revealed the strongest m^{1}Ψ-dependent polysome shift had the highest frequency of codons with uridine in the wobble position (Fig. 5f (left)), and the greatest overall uridine content (Fig. 5f (right)), suggesting that these features correlate with the magnitude of effect induced by the modification. We next assessed the explanatory power of additional sequence features (Fig. 5g and Extended Data Fig. 7f). Notably, codon optimality

accounted for the largest fraction of variance (around 12%), with $m^1\Psi$ effect preferentially associated with non-optimal codons, followed by AU content (around 10%) and uridine percentage (around 9%). The fact that codon optimality (which largely distinguishes codons based on G/C versus A/U in the third position[42]) explains more variance than uridine percentage reinforces the conclusion that $m^1\Psi$ influences translation through direct effects on ribosome dynamics rather than indirectly through a mechanism that depends on overall $m^1\Psi$-content. Consistently, we verified the importance of codon optimality on protein output by conducting luciferase assays comparing UTP and $m^1\Psi$-modified transcripts with low and high codon optimality from our library showing that sequences with low codon optimality exhibited increased protein output from modified mRNA compared with highly optimized sequences (Fig. 5h). These findings support a model in which $m^1\Psi$ exerts its strongest effects in the context of non-optimal codons carrying U in the wobble position, where translation is inefficient and the modification modulates both elongation and initiation dynamics. Overall, $m^1\Psi$ incorporation modulates translation in a sequence-context-dependent manner, underscoring the importance of CDS composition in shaping translation and protein output.

A key conclusion of our study is that $m^1\Psi$ in synthetic mRNA directly modulates translation, enhancing protein output independently of PKR activation and eIF2α phosphorylation. Discrepancies from earlier reports[5] probably reflect RNA preparation quality, as residual by-products of the IVT reaction can activate PKR. Our data show that $m^1\Psi$ directly alters translation dynamics by increasing the ribosome dwell time in specific sequence contexts, namely at NNU P-site codons and NUN A-site codons. These results align with cell-free studies showing that Ψ or $m^1\Psi$ incorporation can locally slow elongation[9,10]. Cryo-EM structures of ribosomes translating $m^1\Psi$-containing mRNAs reveal changes in decoding-centre geometry consistent with reduced elongation speed, providing a structural basis for the context-dependent slowdown observed by ribosome profiling.

Moreover, $m^1\Psi$ enhances translation initiation and protein output, and we identified CDS features that determine the magnitude of the $m^1\Psi$ effect: transcripts with low codon optimality and high U content at the wobble position exhibited the strongest $m^1\Psi$-dependent shift into polysomes. By contrast, highly optimized sequences such as GFP showed little benefit, consistent with a saturation point in ribosome recruitment.

Although initiation is often rate-limiting[43,44], emerging evidence supports an interplay between elongation and initiation[45,46]. In the case of this modification, a mild elongation slowdown may increase local ribosome density and promote recycling[47,48]. Alternatively, initiation may be enhanced through stabilization of pre-organized conformations of the mRNA favourable for initiation factor binding. Future studies will be required to disentangle these possibilities.

In summary, $m^1\Psi$ modifies ribosome dynamics, slowing elongation at specific sites while also promoting initiation, to increase overall protein yield. These findings deepen our understanding of the molecular consequences of mRNA modifications and their relevance for therapeutic applications.

Online content

Any methods, additional references, Nature Portfolio reporting summaries, source data, extended data, supplementary information, acknowledgements, peer review information; details of author contributions and competing interests; and statements of data and code availability are available at https://doi.org/10.1038/s41586-025-09945-5.

1. Saxena, S. et al. The future of mRNA vaccines: potential beyond COVID-19. *Cureus* **17**, e84529 (2025).
2. Anderson, B. R. et al. Nucleoside modifications in RNA limit activation of 2′–5′-oligoadenylate synthetase and increase resistance to cleavage by RNase L. *Nucleic Acids Res.* **39**, 9329–9338 (2011).
3. Karikó, K. et al. Incorporation of pseudouridine into mRNA yields superior nonimmunogenic vector with increased translational capacity and biological stability. *Mol. Ther.* **16**, 1833–1840 (2008).
4. Andries, O. et al. N^1-methylpseudouridine-incorporated mRNA outperforms pseudouridine-incorporated mRNA by providing enhanced protein expression and reduced immunogenicity in mammalian cell lines and mice. *J. Control. Release* **217**, 337–344 (2015).
5. Anderson, B. R. et al. Incorporation of pseudouridine into mRNA enhances translation by diminishing PKR activation. *Nucleic Acids Res.* **38**, 5884–5892 (2010).
6. Bérouti, M. et al. Pseudouridine RNA avoids immune detection through impaired endolysosomal processing and TLR engagement. *Cell* **188**, 4880–4895 (2025).
7. Cerneckis, J., Cui, Q., He, C., Yi, C. & Shi, Y. Decoding pseudouridine: an emerging target for therapeutic development. *Trends Pharmacol. Sci.* **43**, 522–535 (2022).
8. Mulroney, T. E. et al. *N*-Methylpseudouridylation of mRNA causes +1 ribosomal frameshifting. *Nature* **625**, 189–194 (2024).
9. Svitkin, Y. V. et al. N^1-Methyl-pseudouridine in mRNA enhances translation through eIF2α-dependent and independent mechanisms by increasing ribosome density. *Nucleic Acids Res.* **45**, 6023–6036 (2017).
10. Svitkin, Y. V., Gingras, A.-C. & Sonenberg, N. Membrane-dependent relief of translation elongation arrest on pseudouridine- and N1-methyl-pseudouridine-modified mRNAs. *Nucleic Acids Res.* **50**, 7202–7215 (2022).
11. Eyler, D. E. et al. Pseudouridinylation of mRNA coding sequences alters translation. *Proc. Natl Acad. Sci. USA* **116**, 23068–23074 (2019).
12. Monroe, J. et al. N^1-Methylpseudouridine and pseudouridine modifications modulate mRNA decoding during translation. *Nat. Commun.* **15**, 8119 (2024).
13. Baiersdörfer, M. et al. A facile method for the removal of dsRNA contaminant from in vitro-transcribed mRNA. *Mol. Ther. Nucleic Acids* **15**, 26–35 (2019).
14. Ingolia, N. T., Brar, G. A., Rouskin, S., McGeachy, A. M. & Weissman, J. S. The ribosome profiling strategy for monitoring translation in vivo by deep sequencing of ribosome-protected mRNA fragments. *Nat. Protoc.* **7**, 1534–1550 (2012).
15. Leppek, K. et al. Combinatorial optimization of mRNA structure, stability, and translation for RNA-based therapeutics. *Nat. Commun.* **13**, 1536 (2022).
16. Naylor, R., Ho, N. W. & Gilham, P. T. Selective chemical modifications of uridine and pseudouridine in polynucleotides and their effect on the specificities of ribonuclease and phosphodiesterases. *J. Am. Chem. Soc.* **87**, 4209–4210 (1965).
17. Sidrauski, C., McGeachy, A. M., Ingolia, N. T. & Walter, P. The small molecule ISRIB reverses the effects of eIF2α phosphorylation on translation and stress granule assembly. *eLife* **4**, e05033 (2015).
18. Karijolich, J. & Yu, Y.-T. Converting nonsense codons into sense codons by targeted pseudouridylation. *Nature* **474**, 395–398 (2011).
19. Fernández, I. S. et al. Unusual base pairing during the decoding of a stop codon by the ribosome. *Nature* **500**, 107–110 (2013).
20. Adachi, H. & Yu, Y.-T. Pseudouridine-mediated stop codon readthrough in is sequence context-independent. *RNA* **26**, 1247–1256 (2020).
21. Ingolia, N. T., Lareau, L. F. & Weissman, J. S. Ribosome profiling of mouse embryonic stem cells reveals the complexity and dynamics of mammalian proteomes. *Cell* **147**, 789–802 (2011).
22. Rajan, K. S. et al. Structural and mechanistic insights into the function of Leishmania ribosome lacking a single pseudouridine modification. *Cell Rep.* **43**, 114203 (2024).
23. Cappannini, A. et al. MODOMICS: a database of RNA modifications and related information. 2023 update. *Nucleic Acids Res.* **52**, D239–D244 (2023).
24. Holm, M. et al. mRNA decoding in human is kinetically and structurally distinct from bacteria. *Nature* **617**, 200–207 (2023).
25. Milicevic, N., Jenner, L., Myasnikov, A., Yusupov, M. & Yusupova, G. mRNA reading frame maintenance during eukaryotic ribosome translocation. *Nature* **625**, 393–400 (2023).
26. Demeshkina, N., Jenner, L., Westhof, E., Yusupov, M. & Yusupova, G. A new understanding of the decoding principle on the ribosome. *Nature* **484**, 256–259 (2012).
27. Davis, D. R. Stabilization of RNA stacking by pseudouridine. *Nucleic Acids Res.* **23**, 5020–5026 (1995).
28. Kierzek, E. et al. The contribution of pseudouridine to stabilities and structure of RNAs. *Nucleic Acids Res.* **42**, 3492–3501 (2014).
29. Sokoloski, J. E., Godfrey, S. A., Dombrowski, S. E. & Bevilacqua, P. C. Prevalence of syn nucleobases in the active sites of functional RNAs. *RNA* **17**, 1775–1787 (2011).
30. Sonenberg, N., Hershey, J. W. B. & Mathews, M. B. *Translational Control of Gene Expression* (CSHL Press, 2001).
31. Ingolia, N. T., Hussmann, J. A. & Weissman, J. S. Ribosome profiling: global views of translation. *Cold Spring Harb. Perspect. Biol.* **11**, a032698 (2019).
32. Zu, T. et al. Metformin inhibits RAN translation through PKR pathway and mitigates disease in ALS/FTD mice. *Proc. Natl Acad. Sci. USA* **117**, 18591–18599 (2020).
33. Sidrauski, C. et al. Pharmacological brake-release of mRNA translation enhances cognitive memory. *eLife* **2**, e00498 (2013).
34. Boo, S. H. & Kim, Y. K. The emerging role of RNA modifications in the regulation of mRNA stability. *Exp. Mol. Med.* **52**, 400–408 (2020).
35. Lewis, C. J. T. et al. Quantitative profiling of human translation initiation reveals elements that potently regulate endogenous and therapeutically modified mRNAs. *Mol. Cell* https://doi.org/10.1016/j.molcel.2024.11.030 (2024).
36. von der Haar, T. et al. Translation of in vitro-transcribed RNA therapeutics. *Front. Mol. Biosci.* **10**, 1128067 (2023).
37. Jiang, Y. et al. Quantitating endosomal escape of a library of polymers for mRNA delivery. *Nano Lett.* **20**, 1117–1123 (2020).
38. Yanagiya, A. et al. Translational homeostasis via the mRNA cap-binding protein, eIF4E. *Mol. Cell* **46**, 847–858 (2012).
39. Diamond, P. D., McGlincy, N. J. & Ingolia, N. T. Depletion of cap-binding protein eIF4E dysregulates amino acid metabolic gene expression. *Mol. Cell* **84**, 2119–2134 (2024).
40. Yanagiya, A. et al. Requirement of RNA binding of mammalian eukaryotic translation initiation factor 4GI (eIF4GI) for efficient interaction of eIF4E with the mRNA cap. *Mol. Cell. Biol.* **29**, 1661–1669 (2009).

41. Kim, K. Q. et al. N^1-methylpseudouridine found within COVID-19 mRNA vaccines produces faithful protein products. *Cell Rep.* **40**, 111300 (2022).
42. Hia, F. et al. Codon bias confers stability to human mRNAs. *EMBO Rep.* **20**, e48220 (2019).
43. Plotkin, J. B. & Kudla, G. Synonymous but not the same: the causes and consequences of codon bias. *Nat. Rev. Genet.* **12**, 32–42 (2011).
44. Erdmann-Pham, D. D., Dao Duc, K. & Song, Y. S. The key parameters that govern translation efficiency. *Cell Syst.* **10**, 183–192 (2020).
45. Lyons, E. F. et al. Translation elongation as a rate limiting step of protein production. Preprint at *bioRxiv* https://doi.org/10.1101/2023.11.27.568910 (2024).
46. Barrington, C. L. et al. Synonymous codon usage regulates translation initiation. *Cell Rep.* **42**, 113413 (2023).
47. Bonderoff, J. M. & Lloyd, R. E. Time-dependent increase in ribosome processivity. *Nucleic Acids Res.* **38**, 7054–7067 (2010).
48. Afonina, Z. A., Myasnikov, A. G., Shirokov, V. A., Klaholz, B. P. & Spirin, A. S. Conformation transitions of eukaryotic polyribosomes during multi-round translation. *Nucleic Acids Res.* **43**, 618–628 (2015).

Methods

IVT mRNA synthesis

mRNAs were transcribed from linearized plasmids encoding SARS-CoV2 spike, firefly luciferase or GFP using a T7 RNA polymerase kit (MEGAscript T7 Transcription Kit, Thermo Fisher Scientific or HiScribe T7 High Yield RNA Synthesis Kit, NEB) or using the CleanScribe RNA polymerase (E-0107, TriLink Biotechnologies) according to the manufacturer's instructions. For the generation of nucleoside-modified mRNAs, uridine 5′-triphosphate (UTP) was replaced with either the triphosphate derivative of Ψ (ΨTP) (N-1019, TriLink) or $m^1Ψ$ ($m^1Ψ$) (N-1081, TriLink) in the transcription reaction. The RNA was recovered by lithium chloride precipitation. To remove dsRNA, we performed cellulose purification on the IVT RNA according to a method described previously[13]. The IVT RNA was either capped co-transcriptionally with CleanCap Reagent AG (N-7113, TriLink) or enzymatically using the ScriptCap Cap 1 Capping System (CELLSCRIPT) and the poly(A) tail was added for the SARS-CoV2 spike and firefly luciferase transcripts using the A-Plus Poly(A) Polymerase Tailing Kit (CELLSCRIPT). The capped and polyadenylated IVT RNA was purified by ammonium acetate precipitation. The RNA was resuspended in nuclease-free water. The RNA concentration was determined using a Nanodrop spectrophotometer (Thermo Fisher Scientific). To assess quality, the IVT RNA was run on a Tape station (Agilent).

Cell culture

HEK293T cells were cultured in Dulbecco's modified Eagle's medium (DMEM) supplemented with 10% FBS (Sigma-Aldrich) and 2 mM L-glutamine, 100 U ml^{-1} penicillin, 0.1 mg ml^{-1} streptomycin. HEK293T cells with *EIF2AK2*-KO cells were received as a gift from the Ranum Lab[32] and cultured in the same way. *EIF2AK2*-KO cells were validated by immunoblotting for PKR (Extended Data Fig. 5a). Cell lines were confirmed to be free of mycoplasma contamination.

Western blot

For western blot analyses cells were lysed in RIPA buffer (150 mM NaCl, 1% NP-40, 0.5% sodium deoxycholate, 0.1% SDS, 50 mM Tris-HCl pH 7.4 and 1× EDTA-free protease inhibitor cocktail). For phosphorylated proteins, phosphatase inhibitor cocktail 3 (Sigma-Aldrich) was added to the RIPA buffer. Lysates were cleared by centrifugation and supplemented with sample buffer. Proteins were separated by SDS–PAGE electrophoresis, transferred to nitrocellulose membranes (0.25 mm, Thermo Fisher Scientific) and detected using an infrared fluorescent antibody detection system (LI-COR). The primary antibodies used were as follows: spike (Abcam, ab273433, 1:1,000); P-EIF2a (Thermo Fisher Scientific, 44-728G, 1:1,000); EIF2a (Santa Cruz, sc-11386, F-315, 1:1,000); GAPDH (Cell Signaling, 2118, 1:5,000); vinculin (Abcam, 129002, 1:2,000); PKR (Cell Signaling, 3072, 1:1,000); actin (Sigma-Aldrich, A4700, 1:5,000); ATF4 (Cell Signaling, 11815, 1:1,000); firefly-luciferase (Abcam, ab21176, 1:1,000); eIF4E (WB) (Santa Cruz, sc9976, 1:1,000). The secondary antibodies (1:20,000 in TBST and 5% (w/v) skimmed milk powder) used were as follows: IRDye 800CW goat anti-rabbit (Li-COR LIC-926-32211) and IRDye 800CW goat anti-mouse (Li-COR, LIC-926-32210).

Dot blot

RNA (1 µg) was blotted on a positively charged nylon membrane (Amersham Hybond-N+) which was blocked in 5% (w/v) milk in TBS-T for 1 h. Blotted membranes were incubated with J2 anti-dsRNA murine antibody (Scicons, Nordic MUbio) diluted 1:5,000 in blocking buffer. After washing, the membrane was incubated with horseradish-peroxidase-conjugated goat-anti-mouse antibody diluted 1:10,000 in the blocking buffer. Chemiluminescence detection was performed using EZ-ECL, (Sartorius, Biological Industries) and the ImageQuant LAS 4000 (GE Healthcare) imager.

Purification of 80S ribosomes and tRNAs for cryo-EM

Human induced pluripotent stem cells (equivalent to 1.5×10^8 cells) were grown at around 70% confluency. Cell pellets were then collected by centrifugation, and were washed three times in cold buffer C (20 mM HEPES-KOH pH 7.6, 400 mM KOAc, 10 mM $Mg(Oac)_2$, 5 mM putrescine and 5 mM β-mercaptoethanol). Cells were lysed in cold buffer C supplemented with 0.1% Triton X-100, RNase inhibitor and protease inhibitor by three freeze–thaw cycles using liquid nitrogen. Cell debris was removed by centrifugation at 14,000 rpm in a desktop centrifuge. The supernatant was loaded onto a 10–40% (w/v) sucrose gradient in buffer C for centrifugation (22,000 rpm, 11 h, on SW28 rotor, Beckman). The peak corresponding to 80S ribosomes was collected, balanced with buffer C and centrifuged at 55,000 rpm for 12 h at 4 °C. The resulting pellet was suspended in buffer D (20 mM HEPES-KOH pH 7.6, 100 mM KOAc, 10 mM $Mg(Oac)_2$, 10 mM NH4Oac, 5 mM putrescine, 2 mM spermidine and 1 mM dithiothreitol (DTT)) and centrifuged for 90 min at 75,000 rpm (TLA-100 rotor, Beckman). The final ribosome pellet was gently resuspended in buffer D, aliquots were flash-frozen and stored at −80 °C until further use.

To isolate total tRNAs, small RNAs were first enriched by preparing a whole cell lysate by resuspending HEK293 cells (equivalent to 1.5×10^8 cells) in low-salt resuspension buffer (20 mM HEPES-KOH pH 7.6, 25 mM KOAc, 10 mM $Mg(Oac)_2$ and 5 mM β-mercaptoethanol) supplemented with 0.1% Triton X-100, RNase inhibitor and protease inhibitor[49]. Cells were lysed using a Dounce homogenizer. The KOAc concentration in the lysate was gradually increased to 400 mM after continuous stirring in ice for 30 min. Ribosomes were centrifuged for 90 min at 75,000 rpm (TLA-100 rotor, Beckman), and the supernatant was used for small RNA isolation using the standard Trizol/chloroform method. Small RNAs were separated on a 10% polyacrylamide gel, tRNAs (around 70–90 nucleotides) were gel-purified and resuspended in buffer D (20 mM HEPES-KOH pH 7.6, 100 mM KOAc, 10 mM $Mg(Oac)_2$, 10 mM NH_4Oac, 5 mM putrescine, 2 mM spermidine and 1 mM DTT).

Ternary 80S complex formation with mRNA and tRNAs

To reconstitute the classical PRE-ribosome complex with mRNA and three tRNA molecules, we sequentially mixed vacant 80S ribosomes with either modified or unmodified mRNA (13.3 µM) fragment encoding ARG (CGU) and ILE (AUC) codons (CGUAUC, Genscript), 0.33 µM human P-site $tRNA^{Arg}$ (Bio S&T, BH601), 2.66 µM human tRNA mix and 66.6 µM hygromycin B (InvivoGen, ant-hg-1)[22]. The complex assembly was performed at 37 °C in buffer D (20 mM HEPES-KOH pH 7.6, 100 mM KOAc, 10 mM $Mg(Oac)_2$, 10 mM NH_4Oac, 5 mM putrescine, 2 mM spermidine and 1 mM DTT) with a relaxation time of 15 min after the addition of each component.

Cryo-EM data collection and refinement

To prepare cryo-EM grids, 3.5 µl of ribosome suspension (an absorbance at 260 nm (A_{260}) of 13.5) was applied onto glow-discharged holey carbon grids (Quantifoil R2/2) coated with a continuous thin carbon film. The grids were blotted and plunge-frozen using Vitrobot Mark IV (Thermo Fisher Scientific). A Titan Krios electron microscope (Thermo Fisher Scientific) operating at 300 kV equipped with K3 direct electron detector (Gatan) was used for collecting cryo-EM micrographs at liquid nitrogen temperature at a nominal magnification of ×105,000, with a pixel size of 0.8245 Å px^{-1} and a dose rate of around 1 electron per $Å^2$ per frame. Defocus values ranged from −0.6 to −1.7 µm. Relion 5 was used for data processing[50]. Motion correction and contrast transfer function parameters were estimated using Motioncor2[51] and CTFFIND-3[52], respectively. The extracted particles were subjected to several rounds of unsupervised 2D and 3D classification. 3D classes similar to 80S ribosome particles bound to APE tRNAs were selected and subjected to autorefinement in Relion 5 with a blush regularization parameter, which uses a denoising convolutional neural network. After initial

refinement, particles were subjected to CTF refinement, Bayesian polishing and refinement. The resulting high-resolution 3D density map was then subjected to a cycle of multibody refinement using separate masks for the LSU, tRNAs, and the head and body regions of SSU[53]. The gold-standard Fourier shell correlation value criterion of 0.143 was used for determining averaged map resolutions, as implemented in Relion 5.0. Local resolution was estimated using Resmap[54].

Model building and refinement

rRNA and ribosomal protein models were built using template-guided model building in COOT[55]. The coordinate of the human ribosome (PDB: 8GLP) was used as a template for model building and was docked onto density maps using UCSF ChimeraX[56]. The human $tRNA^{Arg}$ (ACG) and $tRNA^{Ile}$ (AAU) sequence was derived from GtRNAdb (https://gtrnadb.org/) and modelled in COOT[55]. (The Mg^{2+}, Zn^{2+}, Na^{+} and K^{+} ion compositions were modelled according to the recently described criteria[57]. Model refinement was performed using an iterative approach, including real-space refinement and geometry regularization in COOT[55], followed by real-space refinement using the PHENIX suite[58]. The final model was validated using MolProbity[14].

Cycloheximide chase assay

Cells were transfected with luciferase encoding IVT mRNA (UTP or $m^1\Psi$) using Lipofectamine 2000 reagent (Thermo Fisher Scientific) and the next day were treated with 100 µg ml^{-1} CHX for 24 h. The samples were collected for western blot analysis at timepoints 6, 9, 12, 18 and 24 h after treatment.

eIF4E RNA IP

Cells transfected with UTP or $m^1\Psi$ luciferase mRNA were collected 8 h after transfection with 1 ml ice-cold RIP lysis buffer (0.4% NP-40, 0.5 mM EDTA pH 8, 100 mM KCl, 20 mM HEPES pH 7.6, 1× protease inhibitor cocktail and 100 U ml^{-1} RNase inhibitor). 10% of the lysates were kept as input samples. Protein A/G PLUS-Agarose beads (Santa Cruz, sc-2003) were washed three times in RIP wash buffer (50 mM Tris pH 7.4, 150 mM NaCl, 1 mM $MgCl_2$, 0.05% NP-40, 100 U ml^{-1} RNase inhibitor) before being incubated with 2 µg anti-eIF4E antibody (Y448) (Abcam, ab33766-100) per sample and rotated for 4 °C for 3 h. Antibody-bound beads were gently washed three times and added to lysates for IP, and the samples were incubated overnight with rotation at 4 °C. IP samples were then gently centrifuged and unbound fractions were separated. IP bound beads were washed five times in RIP wash buffer before western blotting and RNA isolation were performed.

IP and MS

HEK293T cells were transfected with spike encoding IVT mRNA (UTP, ΨTP or $m^1\Psi$) using Lipofectamine 2000 (Thermo Fisher Scientific) transfection reagent. Cells were lysed with freshly prepared lysis buffer (150 mM NaCl, 50 mM Tris HCl pH 7.5, 1% NP40, 1 mM $MgCl_2$, 1× protease inhibitor (P2714, Sigma-Aldrich), 1× phosphatase inhibitor (P0044, Sigma-Aldrich)). Protein A/G PLUS-agarose beads (Santa Cruz, sc-2003) were washed three times with 500 µl lysis buffer and then incubated with 5 µg of anti SARS-CoV spike glycoprotein antibody (Abcam, ab273433) for 5 h at 4 C. Next, the A/G beads with antibody mixture was washed three times and 4 mg total protein per sample was loaded onto A/G agarose beads for overnight incubation. The samples were then washed three times with ice cold wash buffer I (150 mM NaCl, 50 mM Tris HCl (pH 7.5), 0.05% NP40) followed by three washes with ice-cold wash buffer II (150 mM NaCl, 50 mM Tris HCl (pH 7.5)) to remove detergents. The tubes were rotated for efficient washing. Immunoprecipitated spike protein was eluted by adding 100 µl elution buffer I (2 M urea, 50 mM Tris-HCl (pH 7.5), 1 mM DTT) and 1 µl trypsin (0.4 µg $µl^{-1}$) to each sample. The samples were placed in a room temperature shaker for 2 h before centrifugation and the supernatant was collected to a clean tube. Then, 100 µl elution buffer II (2 M urea, 50 mM Tris-HCl (pH 7.5), 5 mM CAA) was added to the samples for an additional 5 min at room temperature with shaking before centrifugation and collecting the supernatant. Digestion continued overnight at room temperature. Digestion was stopped using 1 µl trifluoroacetic acid.

The liquid chromatography–MS (LC–MS) analyses were performed using a Dionex UltiMate RSLC 3000 nano-HPLC system coupled to an Exploris480 mass spectrometer (Thermo Fisher Scientific), using two data-dependent acquisition methods with FAIMS gas-phase fractionation at compensation voltages of −40 V and −60 V, or −50 V and −65 V. Peptides were loaded onto the Acclaim PepMap 100 µm x 2 cm C18 precolumn (Thermo Fisher Scientific) and separated on the PepMap RSLC C18, 2 µm, 100 A, 75 µm × 75 µm analytical column (Thermo Fisher Scientific) maintained at 40 °C. Full scans were acquired across a mass range of 350–1,200 *m*/*z*. The MS1 resolution was set to 60,000, with a custom automatic gain control (AGC) target normalized to 300%. The MS2 resolution was set to 15,000, using a standard AGC target. Precursors with charge states from 2 to 6 were selected for fragmentation using a normalized HCD collision energy of 30%. The cycle time between master scans was set to 1.5 s for both FAIMS CVs. A 180-min gradient elution was used at a flow rate of 0.200 µl min^{-1}, with solvent B (80% acetonitrile, 0.1% formic acid) increasing from 4% to 12% over 2 min; then to 28% at 145 min; 44% at 146 min; and 85% at 150 min; before returning to 4% for re-equilibration.

The 2 CV raw files were split using Freestyle 1.8 SP2 (Thermo Fisher Scientific) and analysed as fractions of a single sample using Maxquant (v.2.4.2.0) against a spike protein reference sequence (NCBI: BCN86353.1) and an in silico-derived spike protein library containing all single, double and triple substitution products for each nucleotide and neighbouring codons in separate FASTA files.

RT–qPCR

Tri-Reagent (Sigma-Aldrich) was used for total RNA extractions using chloroform phase separation. cDNA was prepared from 0.5 µg total RNA using the qScript FLEX cDNA Synthesis Kit with random primers (Quanta Biosciences) according to the manufacturer's instructions. qPCR was performed using the SYBR Green PCR master-mix (ABI) on the QuantStudio 12K Flex (ABI) with the following primers (forward, reverse): luciferase (ACACCCGAGGGGGATGATAA, GGCGACGTAATCC ACGATCT); spike (GTGCGTGAACCTGACCA, AGAGCCAGCAGTGTCT); GFP 5′ UTR (TCTTCTGGTCCCCACAGACT, CTCGCCCTTGCTCACCAT).

Fractionation assay

HEK293T cells were transfected with IVT luciferase mRNA (UTP or $m^1\Psi$) using Lipofectamine 200 reagent (Thermo Fisher Scientific) and, the next day, were washed in PBS, trypsinized and resuspended in cold PBS. A fraction of 10% of the cells was then transferred to a new tube and RNA was extracted in Tri-reagent to obtain whole cellular extract. The remaining cells were pelleted for 5 min at 300*g*. Cells were resuspended in 150 µl fractionation buffer A (15 mM Tris-Cl pH 8, 15 mM NaCl, 60 mM KCl, 1 mM EDTA pH 8, 0.5 mM EGTA pH 8, 0.5 mM spermidine and 10 U ml^{-1} RNase inhibitor), and 150 µl 2× lysis buffer (15 mM Tris-Cl pH 8, 15 mM NaCl, 60 mM KCl, 1 mM EDTA pH 8, 0.5 mM EGTA pH 8, 0.5 mM spermidine, 10 U ml^{-1} RNase inhibitor and 0.5% NP-40) was added followed by 10 min incubation on ice. The extract was pelleted for 5 min at 400*g* and the supernatant containing the cytoplasmic fraction was removed to a new tube. This was centrifuged again at 500*g* for 1 min, the supernatant was transferred to a new tube and RNA was extracted with Tri-reagent. The membranous and nuclear pellet was resuspended in 1 ml RLN buffer (50 mM Tris-Cl pH 8, 140 mM NaCl, 1.5 mM $MgCl_2$, 0.5% NP-40, 10 mM EDTA and 10 U ml^{-1} RNase inhibitor) and incubated on ice for 5 min. The membranous and nuclear fraction was then pelleted for 5 min at 500*g*, the supernatant was removed and RNA was extracted from the pellet with Tri-reagent. RT–qPCR was performed as described above.

Flow cytometry

GFP and mCherry (normalizing control) expression was measured by flow cytometry. Cells were washed in PBS and filtered through a 40-µm nylon mesh. Flow cytometry analysis was performed on the CytoFLEX S flow cytometer (Beckman Coulter) and analysed using FlowJo.

Luciferase assay

Cells were transfected with IVT luciferase mRNA (UTP, ΨTP or $m^1Ψ$) using Lipofectamine 2000 reagent (Thermo Fisher Scientific) and the next day the luciferase activity was determined using the Dual-Glo Luciferase Assay System (Promega) according to the manufacturer's protocol and measured on the GloMax (Promega) Microplate reader (Promega).

Polysome profiling

24 h after transfection of IVT mRNA (UTP or $m^1Ψ$) using Lipofectamine 2000 reagent (Thermo Fisher Scientific), HEK293T cells were treated with 100 µg ml^{-1} CHX for 1 min and then washed with cold PBS with 100 µg ml^{-1} CHX. Cells were scraped and lysed with 250 µl lysis buffer (1% Triton X-100 in 20 mM Tris pH 7.5, 150 mM NaCl, 5 mM $MgCl_2$, 1 mM DTT supplemented with 10 U ml^{-1} Turbo DNase and 100 µg ml^{-1} CHX). The lysed samples were vortexed and centrifuged at 12,000*g* at 4 °C for 10 min. The cleared lysates were loaded onto 10–50% sucrose gradients prepared using BioComp Gradient Maker and centrifuged at 35,000 rpm in a SW41 rotor for 3 h at 4 °C. The gradients were fractionated, and the optical density at 254 nm was continuously recorded using the BioComp fractionator. Peaks corresponding to 40S, 60S and 80S were identified and polysomes, represent mRNAs actively engaged in translation by multiple ribosomes, were further subdivided to two groups according to their sedimentation position. The fractions located just beyond the 80S monosome peak correspond to light polysomes (few ribosomes per mRNA), while fractions sedimenting further down the gradients represent heavy polysomes (many ribosomes per mRNA). RNA was extracted from the fractions using 8 M guanidine hydrochloride (Sigma-Aldrich) followed by RT–qPCR. Alternatively, RNA extracted from each fraction was reverse transcribed, and the barcode regions of the luciferase library were specifically amplified using primers containing Illumina-compatible overhangs. The resulting amplicons were pooled and subjected to deep sequencing to quantify barcode distributions across polysome fractions.

Ribosome-profiling and RNA-seq library preparation

Cells were washed with ice cold PBS and then immediately frozen in liquid nitrogen or pretreated with harringtonine (2 mg ml^{-1}) and cycloheximide (100 mg ml^{-1}). Cells were scraped from 10-cm plates on ice and in the presence of 500 µl lysis buffer (1% Triton X-100 in 20 mM Tris pH 7.5, 150 mM NaCl, 5 mM $MgCl_2$, 1 mM DTT supplemented with 10 U ml^{-1} Turbo DNase and 100 µg ml^{-1} CHX). After lysis, the samples stood on ice for 20 min and were then centrifuged at 14,000*g* for 15 min to remove cell debris. The supernatants were split into two tubes—one for RNA-seq and one for Ribo-seq library preparation. The RNA-seq samples were treated with Tri-Reagent (Sigma-Aldrich), total RNA was extracted using chloroform phase separation, and poly(A) selection was performed using the Dynabeads mRNA DIRECT Purification kit (Invitrogen). mRNA samples were subjected to DNase I treatment and 3′ dephosphorylation using FastAP thermosensitive alkaline phosphatase (Thermo Fisher Scientific) and T4 PNK (NEB) followed by 3′ adaptor ligation using T4 ligase (NEB). The ligated products were used for reverse transcription with SSIII (Invitrogen) for first-strand cDNA synthesis. The cDNA products were 3′ ligated with a second adaptor using T4 ligase and amplified with 8 cycles of PCR for final library products of 200–300 bp. Ribo-seq samples were treated with RNase I for 45 min at room temperature followed by SUPERase-In (Invitrogen) quenching. Subsequent Ribo-seq library generation was performed as previously described[14]. In brief, the digested samples were loaded onto a sucrose solution (34% sucrose, 20 mM Tris pH 7.5, 150 mM NaCl, 5 mM $MgCl_2$, 1 mM DTT and 100 µg ml^{-1} CHX) and centrifuged for 1 h at 100,000 rpm in a TLA-110 rotor (Beckman) at 4 °C. The pellet was collected using TRI reagent (Sigma-Aldrich) and the RNA was extracted using chloroform phase separation. For size selection, 15 µg total RNA was separated on a 15% TBE-urea gel for 65 min, and 28–34 footprints were excised using 28 and 34 flanking RNA oligos, followed by RNA extraction and rRNA depletion (NEBNext rRNA Depletion Kit v2) and subsequent Ribo-seq protocol[14].

Sequence alignment and metagene analysis

Sequencing reads were aligned as previously described[59]. In brief, linker (CTGTAGGCACCATCAAT) and poly(A) sequences were removed and the remaining reads were aligned to the *Homo sapiens* (human) genome assembly hg19 or to the spike and luciferase sequences. Alignment was performed using Bowtie v.1.1.229 with a maximum of two mismatches per read. Reads that were not aligned to the genome were aligned to the transcriptome. The aligned position on the genome was determined as the 5′ position of RNA-seq reads, and for Ribo-seq reads, the P-site of the ribosome was calculated according to reads length using the offset from the 5′ end of the reads that was calculated from cellular ORFs. The offsets used are +12 for reads that were 28–29 bp and +13 for reads that were 30–33 bp. Reads that were different in length were discarded. In all of the figures presenting ribosome-density data, all footprint lengths (28–33 bp) are presented. For metagene analysis only genes with CDS length of at least 300 nucleotides and more than 50 reads were used. For each gene, normalization was done to its maximum signal and each position was normalized to the number of genes contributing to the position. For calculating ribosome densities comparing transcript and footprint expression level, RNA and footprint counts from bowtie alignments were normalized to units of RPKM to normalize for gene length and for sequencing depth. For codon resolution analysis of spike and luciferase gene, the PRICE[60] pipeline was used applying the default parameters and filtering for uniquely aligned reads to ensure accurate frame assignment. Each replicate of a given sample was run separately.

Ribosome-depletion assay analysis

Metagene profiles from Harringtonine run-off experiments were generated by aligning ribosome footprint reads relative to annotated start codons. To account for global differences in coverage, each profile was further normalized to the median ribosome density measured over 500 codons that remained largely unaffected by the Harringtonine treatment times used in this study. For depletion analysis, ribosome densities at each codon position were expressed as a ratio relative to the 0 s (untreated) timepoint, providing a measure of relative ribosome loss over time. To reduce noise and visualize the depletion kinetics, the resulting profiles were smoothed using locally weighted scatterplot smoothing (LOWESS) with a span parameter of 0.5.

Frameshift analysis

The analysis was conducted on the combined sum of reads from two replicates for each condition (UTP and $m^1Ψ$) separately.

Step 1: baseline reading frame distributions. To establish a baseline for read distributions in different reading frames, we used randomization to calculate the mean and s.d. of the fraction of reads in each reading frame. We performed these calculations across a range of window sizes (5–100 bp) to match the actual variability in window lengths that were analysed. For each iteration, we randomly sampled reads from each reading frame across the full transcript (spike or luciferase) and computed the fraction of reads in each frame. This process was repeated 1,000 times, enabling us to determine the mean and s.d. for each reading frame.

Step 2: *Z*-score calculation for frameshifting. Slippery sites were defined as codons where a +1 frameshift results in a codon encoding the same amino acid. For each potential slippery site, we identified the corresponding slippery window—the interval extending from the slippery site to the next stop codon in the +1 reading frame. For each slippery window, we calculated the fraction of reads in each reading frame. Using the mean and s.d. obtained in step 1, we then computed the *Z* score for each reading frame to assess deviations from the expected distribution.

Step 3: simulating +1 frameshifting. To simulate different levels of +1 frameshifting, we performed computational experiments with increasing percentages of frameshifting: 1, 2, 3, 5, 10, 20, 50 and 100%. For a given frameshift percentage *P*, we adjusted the read distribution for each reading frame *R* by sampling reads from both *R* and the +1 reading frame as follows:

$$\text{Reads at frame } R \text{ under frameshift level } P = (1-P) \times \text{reads from } R + P \times \text{reads from } R+1$$

This simulation was repeated 1,000 times, using window lengths matching those of the slippery windows identified in step 2. For each iteration, we computed the *Z* score for each reading frame. We then calculated the mean and median *Z* score across all windows. The distribution of these median *Z* scores from the 1,000 simulations was compared to the actual *Z* scores obtained in step 2 to assess frameshifting likelihood.

Steps 2 and 3 were conducted separately for slippery sites that contained U in the P-site codon or contained U in the A-site codon (one codon downstream) or sites that did not contain U in either of these positions.

Alternative analysis using DESeq2-identified codons. In addition to analysing predefined slippery sites, we repeated steps 2 and 3 using codon positions identified as significant in DESeq2 differential expression analysis, indicating these sites lead to slow elongation. We treated these sites as potential frameshift hotspots, repeating the above analysis.

Reporting summary

Further information on research design is available in the Nature Portfolio Reporting Summary linked to this article.

Data availability

All next-generation sequencing data files have been deposited at the Gene Expression Omnibus under accession GSE309271. The cryo-EM density maps of the ribosome complexes have been deposited in the Electron Microscopy Data Bank under accession numbers EMD-55091 and EMD-55083. Atomic coordinates and structure factors have been deposited in the PDB under accession codes 9SPI and 9SPF.

49. Rajan, K. S. et al. Identification and functional implications of pseudouridine RNA modification on small noncoding RNAs in the mammalian pathogen *Trypanosoma brucei*. *J. Biol. Chem.* **298**, 102141 (2022).
50. Zivanov, J. et al. New tools for automated high-resolution cryo-EM structure determination in RELION-3. *eLife* **7**, e42166 (2018).
51. Zheng, S. Q. et al. MotionCor2: anisotropic correction of beam-induced motion for improved cryo-electron microscopy. *Nat. Methods* **14**, 331–332 (2017).
52. Mindell, J. A. & Grigorieff, N. Accurate determination of local defocus and specimen tilt in electron microscopy. *J. Struct. Biol.* **142**, 334–347 (2003).
53. Kucukelbir, A., Sigworth, F. J. & Tagare, H. D. Quantifying the local resolution of cryo-EM density maps. *Nat. Methods* **11**, 63–65 (2014).
54. Emsley, P., Lohkamp, B., Scott, W. G. & Cowtan, K. Features and development of Coot. *Acta Crystallogr. D* **66**, 486–501 (2010).
55. Pettersen, E. F. et al. UCSF ChimeraX: structure visualization for researchers, educators, and developers. *Protein Sci.* **30**, 70–82 (2021).
56. Leonarski, F., Henning-Knechtel, A., Kirmizialtin, S., Ennifar, E. & Auffinger, P. Principles of ion binding to RNA inferred from the analysis of a 1.55 Å resolution bacterial ribosome structure—Part I: Mg^{2+}. *Nucleic Acids Res.* **53**, gkae1148 (2025).
57. Afonine, P. V. et al. Real-space refinement in PHENIX for cryo-EM and crystallography. *Acta Crystallogr. D* **74**, 531–544 (2018).
58. Williams, C. J. et al. MolProbity: more and better reference data for improved all-atom structure validation. *Protein Sci.* **27**, 293–315 (2018).
59. Tirosh, O. et al. The transcription and translation landscapes during human cytomegalovirus infection reveal novel host-pathogen interactions. *PLoS Pathog.* **11**, e1005288 (2015).
60. Erhard, F. et al. Improved Ribo-seq enables identification of cryptic translation events. *Nat. Methods* **15**, 363–366 (2018).

Acknowledgements We thank I. Ulitsky, S. Schwartz and the members of the Stern-Ginossar laboratory for reading the manuscript; and Y. Lubelsky for technical assistance. B.R. is supported by the Ariane de Rothschild Women's Doctoral Program. K.S.R. is supported by the Senior-Postdoctoral Fellowship from the Weizmann Institute of Science. A.Y. holds the Martin S. and Helen Kimmel Professorial Chair at the Weizmann Institute of Science. Work in the Stern-Ginossar group is supported by a European Research Council consolidator grant (CoG-2019-864012). This project was funded by the Abisch-Frenkel RNA Therapeutics Center.

Author contributions B.R. and N.S.-G. conceived and designed the project. B.R., K.B. and T.A. performed the molecular biology experiments. K.S.R., C.S., E.W., A.Y. and A.B. acquired and interpreted the cryo-EM data. B.R. and A.N. analysed the deep sequencing data. V.M. and T.G. conducted and interpreted the MS measurements. C.J.W. and J.M.R. provided critical reagents and protocols. B.R., K.S.R. and N.S.-G. wrote the manuscript with critical input from all of the authors.

Competing interests The authors declare no competing interests.

Additional information

Supplementary information The online version contains supplementary material available at https://doi.org/10.1038/s41586-025-09945-5.

Correspondence and requests for materials should be addressed to Batsheva Rozman or Noam Stern-Ginossar.

Peer review information *Nature* thanks Jeff Coller, Nahum Sonenberg and the other, anonymous, reviewer(s) for their contribution to the peer review of this work. Peer reviewer reports are available.

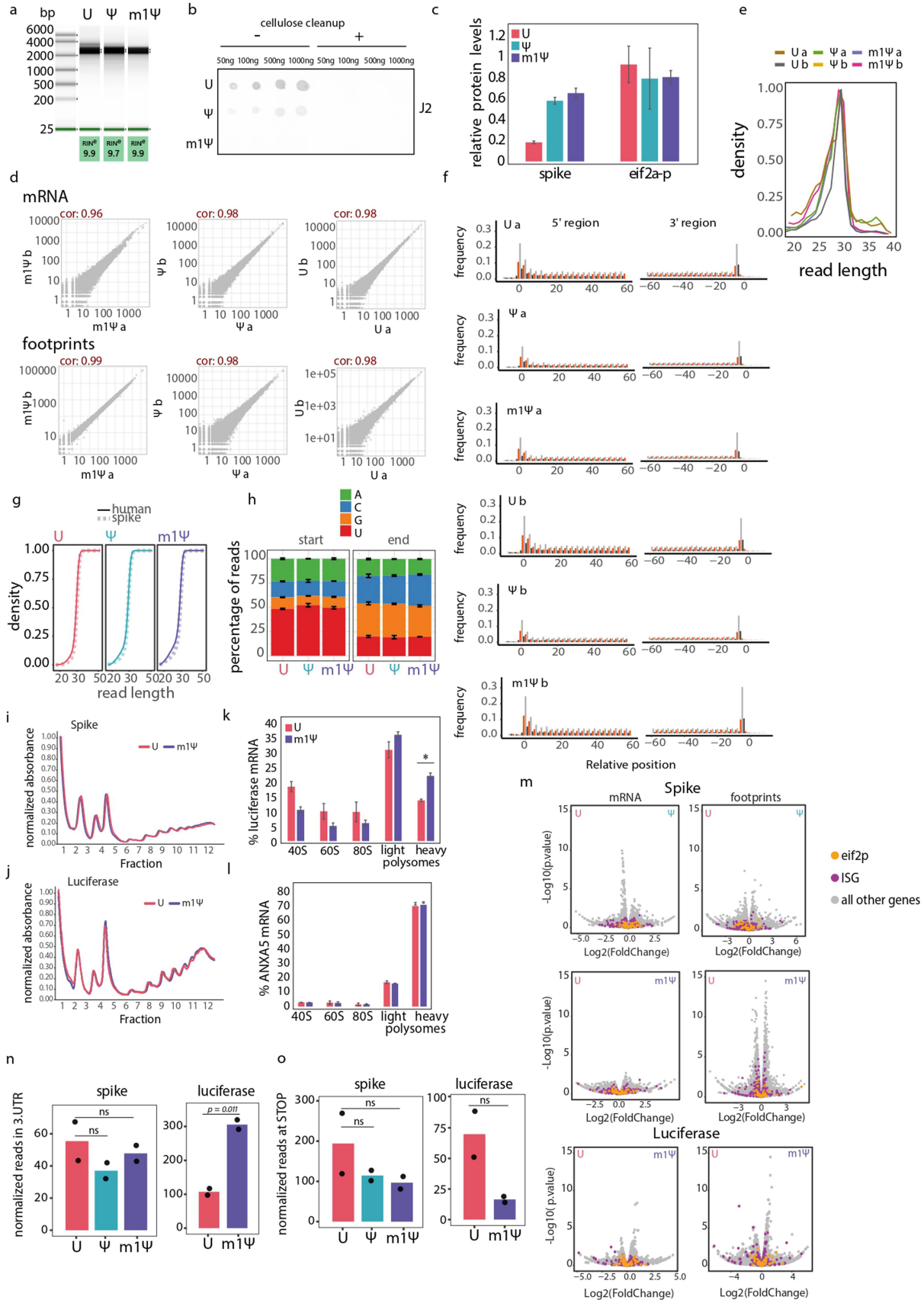

Extended Data Fig. 1 | See next page for caption.

Extended Data Fig. 1 | Modified mRNA has increased ribosome load. **a**, TapeStation analysis of IVT spike mRNAs containing UTP, Ψ, or $m^1\Psi$. **b**, Dot blot of IVT Spike mRNAs containing UTP, Ψ, or $m^1\Psi$, probed with the J2 antibody to detect dsRNA, shown before and after cellulose cleaning. **c**, Quantification of Spike (relative to gapdh) and phosphorylated eIF2α (relative to eIF2α levels) measured by western blot (Fig. 1b) error bars show s.d. of two replicates. **d**, Scatter plots showing transcript expression in biological replicates of RNA-seq (top panels) and ribosome profiling (bottom panels). Spearman correlation is depicted at the top of each graph. **e**, Density plot showing ribosome footprint read length distributions. **f**, Meta gene analysis of ribosome profiling libraries around the Start codon and Stop codons. Each frame (−1, 0, +1) is labelled in red, grey, or black bars correspondingly. **g**, Cumulative plots depicting read lengths for human or spike footprints. **h**, Stacked box plots depicting proportion of reads that start (left panels) or end (right panels) with each nucleotide for spike ribosome footprints. **i**,**j**, Polysome profiles of 293T cells transfected with UTP or $m^1\Psi$ Spike IVT mRNAs (**i**) or with UTP or $m^1\Psi$ luciferase IVT mRNAs (**j**). Profiles depict averaged absorbance across three biological replicates and normalized to minimum absorbance values. X-axis depicts the 12 fractions that were collected. **k**,**l**, The relative distribution of luciferase mRNA (**k**) and *ANXA5* mRNA, endogenous control transcript (**l**), across polysome fractions. RNA from 12 gradient fractions (presented in **j**) and quantified by RT-qPCR. Bars represent the mean and s.d. of three biological replicates. **m**, Volcano plots of differentially expressed genes (mRNA) and differentially translated genes (ribosome footprints) in cells transfected with UTP or modified spike or luciferase mRNAs. eIF2α phosphorylation dependent genes[17] (yellow) and ISGs (magenta) are highlighted. Y-axis denotes -log10 p.values and X-axis shows log2 transformed fold change values. **n**,**o**, Bar plots showing ribosome footprint reads mapping to the 3′UTR (**n**) or to Stop codon (**o**) of spike and luciferase mRNAs, normalized to reads mapping to the respective CDS. Individual data points represent each replicate. P-value calculated using standard two-sided t-test.

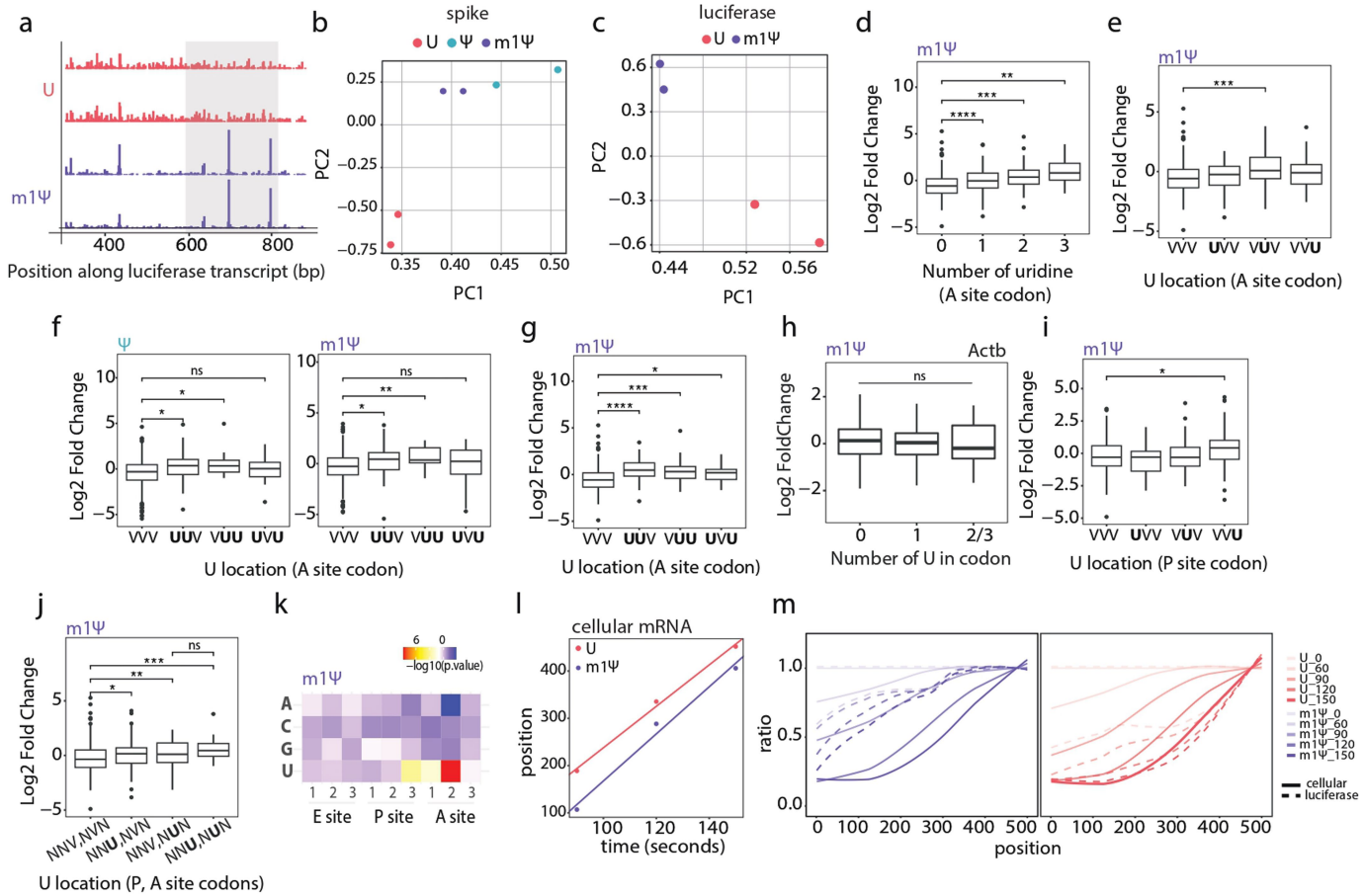

Extended Data Fig. 2 | Modified nucleotides slow translation elongation in specific sequence context. a, Ribosome footprint profiles along a segment of the luciferase mRNA from UTP or m^{1}Ψ modified transcripts. Bars depict read coverage at every nucleotide. Grey squares highlight differences in profiles between samples. **b,c**, PCA analysis of codon level ribosome densities in spike (**b**) and luciferase (**c**) IVT mRNA containing either UTP Ψ and m^{1}Ψ (spike) or UTP and m^{1}Ψ (luciferase) at 24 h post transfection into 293T cells. **d-j**, Boxplot depicting the log2 -transformed fold change of relative ribosome densities of modified mRNA compared to non-modified in codons along luciferase mRNA (d,e,g,i and j) or spike mRNA (f) binned by number of uridines in the A-site (**d**), by the location of uridine in the A-site (**e**, **f** and **g**), in the endogenous transcript Actin b (**h**), by the location of uridine in the P-site codon (**i**) by location of uridine in the A-site codon and P-site codons (**j**). V represents non-uridine bases. p.values were calculated using two-sided standard t-test. **k**, Heatmap showing the −log10-transformed P values from nucleotide enrichment tests at each position (E,P,A site) on luciferase mRNA where ribosome densities differ significantly between m1Ψ and UTP. Positive values indicate enrichment whereas negative values indicate depletion compared to UTP. **l**, Rate of ribosome depletion. The codon position of 50% ribosome depletion is plotted as a function of harringtonine treatment time (seconds) for cellular transcripts in cells transfected with UTP luciferase mRNA (red) or m^{1}Ψ modified luciferase mRNA (blue). **m**, Metagene analysis of run-off elongation at distinct time points (treatment time is denoted in Fig legend : 0, 60, 90, 120, 150 s) for cellular genes (solid line) and luciferase gene (dashed line) from UTP luciferase (red, right panel) or m^{1}Ψ luciferase (blue, left panel) mRNAs transfected cells. Ribosome read densities are shown as ratios relative to the untreated 0-timepoint and curves were smoothed using a locally weighted regression with a smoothing parameter (span) of 0.5.

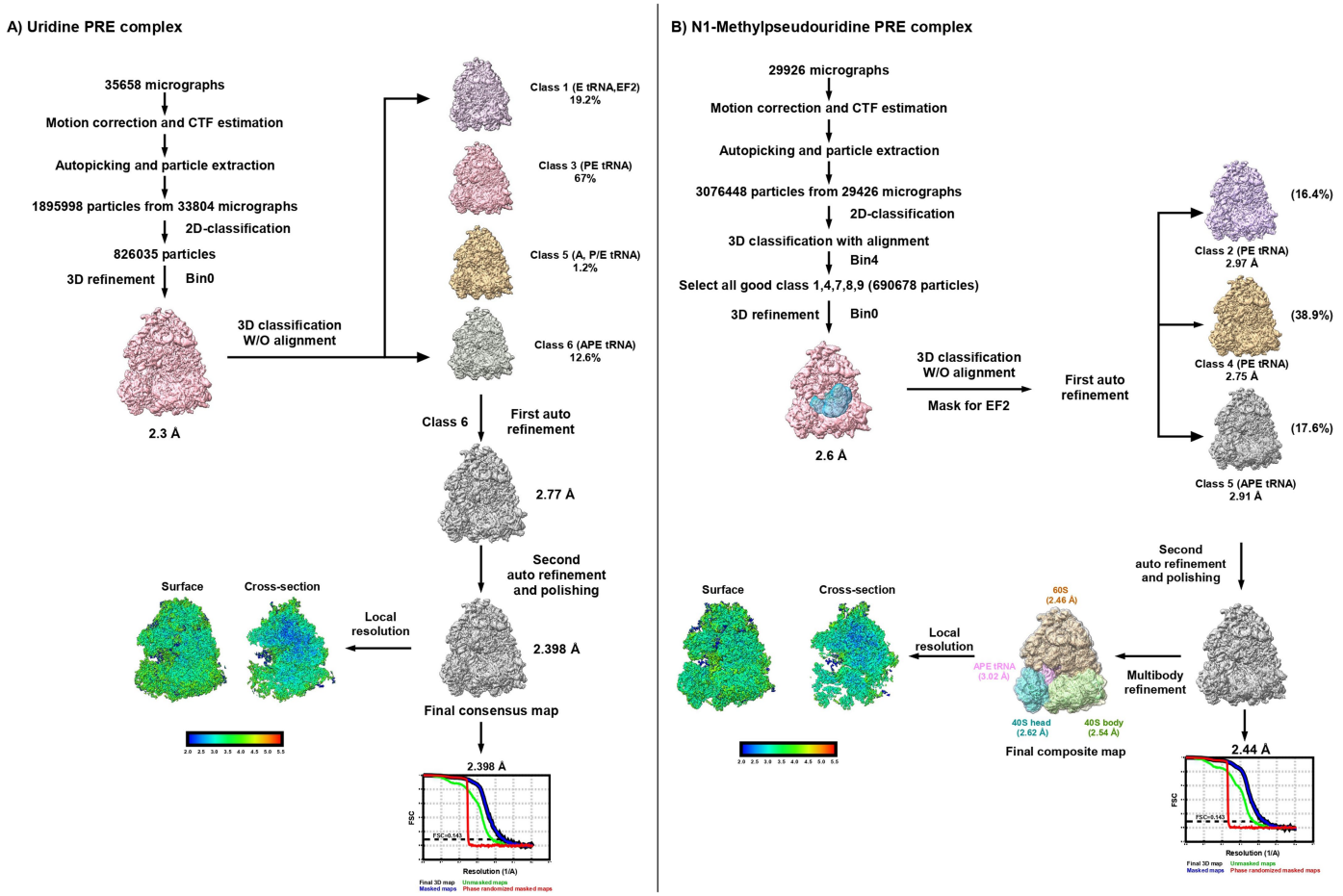

Extended Data Fig. 3 | Cryo-EM data processing pipeline used to reconstruct EM maps. Flow chart presenting the outline of the cryo-EM data processing pipeline used to reconstruct the EM map. The number of micrographs, particles, 3D classes obtained, and the resolution of corresponding maps are indicated. "Gold standard" FSC curves for the consensus EM map (black), unmasked map (green), masked map (blue), and phase randomized masked map (red) are presented. Surface rendering and cross-section of the cryo-EM density maps are coloured according to local resolution distribution. **a**, Uridine-PRE ribosomes. **b**, $m^1\Psi$-PRE ribosomes.

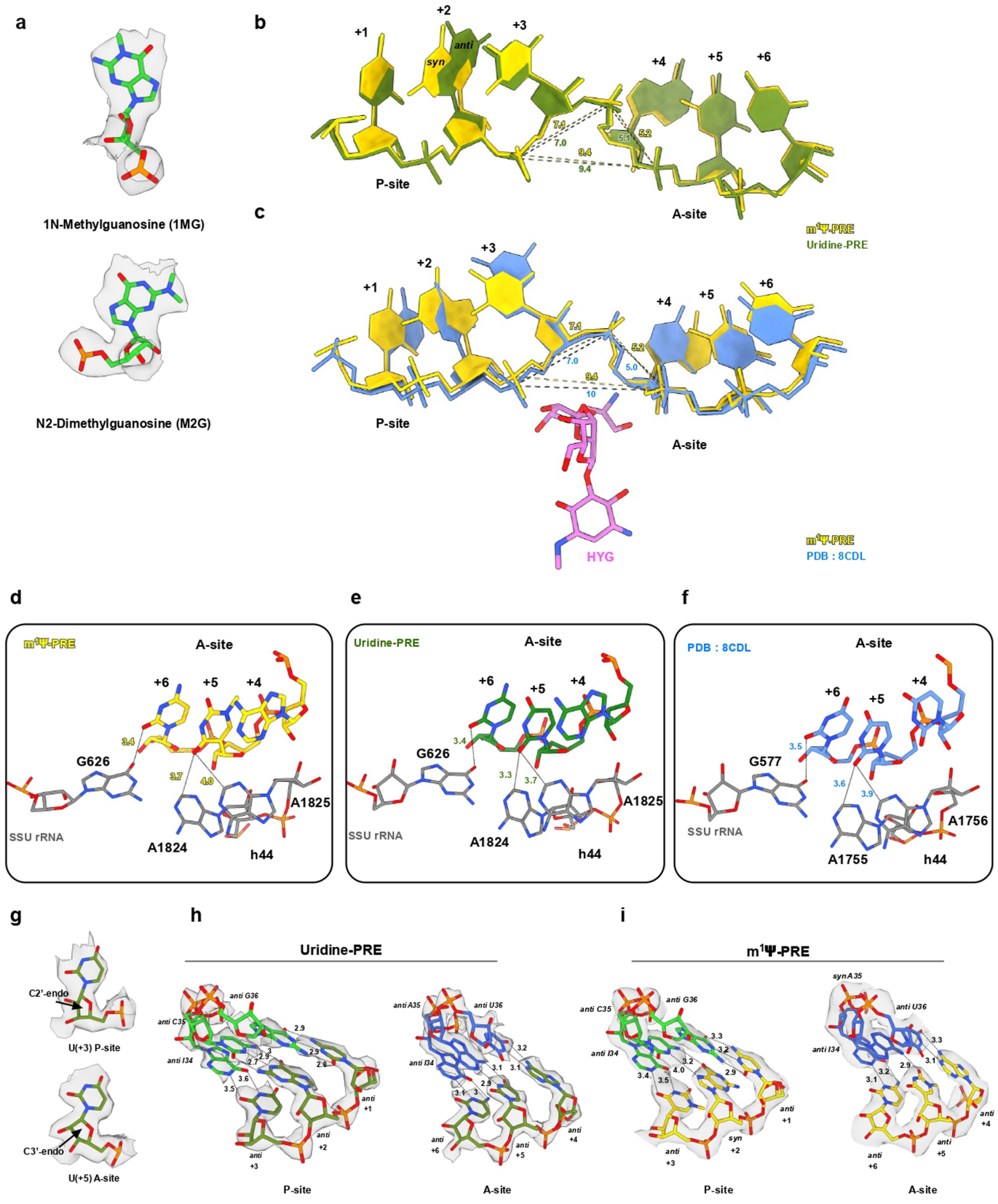

Extended Data Fig. 4 | See next page for caption.

Extended Data Fig. 4 | Cryo-EM analysis of Uridine-PRE and m$^1\Psi$-PRE ribosome structures. a, Examples of RNA modification visualized in the P-site tRNA^{Arg}. The EM map and the corresponding model are superimposed. The identity of the RNA modification and its PDB ligand ID is indicated. **b**,**c**, Superimposition of the mRNA nucleotides in Human Uridine-PRE, m$^1\Psi$-PRE, and Yeast PRE complexes. The distances between the phosphate group near the A/P kink are indicated. **b**, Comparison between m$^1\Psi$-PRE and Uridine-PRE complexes. **c,** Comparison between m$^1\Psi$-PRE with hygromycin and yeast-PRE (PDB: 8CDL) without hygromycin complexes. **d**–**f**, Comparison of the distances between SSU rRNA nucleotides and the A-site mRNA nucleotides in Human Uridine-PRE, m$^1\Psi$-PRE, and Yeast-PRE (PDB: 8CDL) complexes. The distances between the A-site nucleotide and SSU rRNA nucleotides are indicated. **(d)** m$^1\Psi$-PRE complex, **(e)** Uridine-PRE complex, and **(f)** Yeast-PRE complex. **g**, Sugar puckers of the two Uridine nucleotides in Uridine-PRE complex. The cryo-EM density of the Uridine in +3 and +5 positions is shown. **h**, **i**, Codon-anticodon base-pairing in the Uridine-PRE complex. **(h)** Watson Crick (WC) base-pair interactions in the P-site and A-site nucleotides of the Uridine-PRE complex. The EM map of mRNA and tRNA nucleotides in the P-site and A-site is shown to indicate the nucleobase *anti*-conformation of G(+ 2) and *anti*-conformation of A35, respectively. The distances of the observed hydrogen bonds between the codon-anticodon are indicated. **(i)** Same as in (h) for m$^1\Psi$ -PRE complex. The EM map of mRNA and tRNA nucleotides in the P-site and A-site is shown to indicate the nucleobase *syn*-conformation of G(+ 2) and *syn*-conformation of A35, respectively.

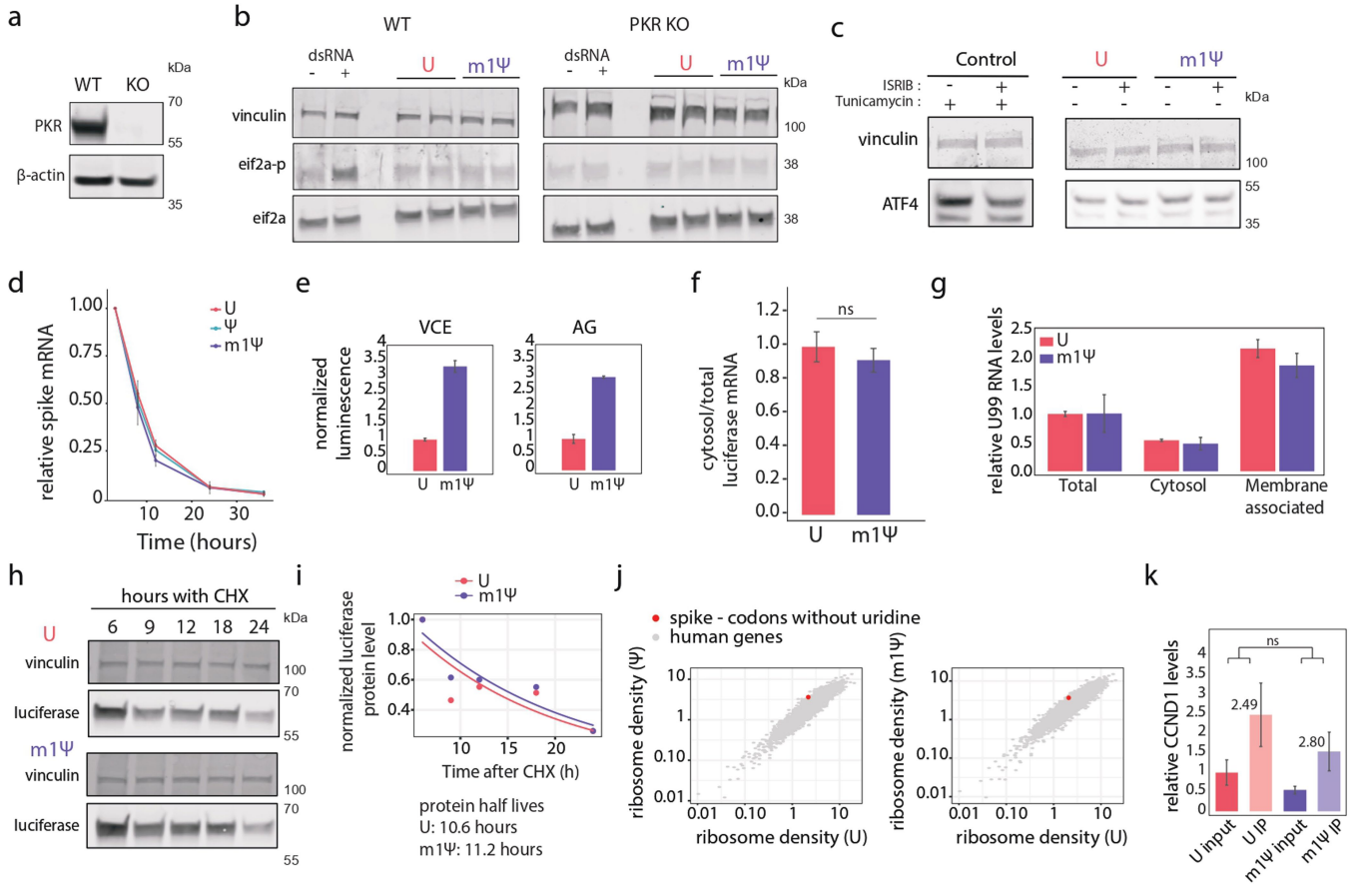

Extended Data Fig. 5 | Enhanced translation initiation underlies increased expression of m^{1}Ψ-modified mRNAs. a, Western blot showing PKR expression levels in WT 293T compared to *EIF2AK2*-KO 293T cells. β-actin is shown for loading control. **b**, Western blot analysis for eIF2α phosphorylation levels in WT 293T (left panel) or *EIF2AK2*-KO 293T (right panel) cells transfected with UTP or m^{1}Ψ modified mRNA. dsRNA was used as a positive control for PKR induction. Vinculin is shown. **c**, Western blot analysis for ATF4 levels in cells transfected with UTP or m^{1}Ψ modified mRNA and treated with ISRIB. Tunicamycin was used as a control for ATF4 induction and ISRIB activity, vinculin loading control is shown. **d**, Relative spike mRNA levels at various time points following transfection with mRNAs containing UTP, Ψ, or m^{1}Ψ. Levels were measured by RT-qPCR and normalized to housekeeping gene (*ANXA5*). Data represent mean and s.d. of three biological replicates. **e**, Bar plots depicting firefly luciferase luminescence normalized to Renilla control of UTP (red) or m^{1}Ψ modified (blue) mRNA prepared with two different capping mechanisms - vaccinia virus capping enzyme (VCE, left) or co-transcriptional cap1 analog (AG, right). Error bars depict s.d. of three biological replicates. **f**, Bar plot depicting luciferase mRNA levels in cytosol fraction compared to total cell lysate as measured by RT-qPCR and normalized to *ANXA5* gene. Data represent average and s.d. of 3 biological replicates. Statistical significance was calculated by two-sided standard t. test. **g**, Relative U99 RNA expression normalized to *ANXA5* gene as measured by RT-qPCR from each fraction (total, cytosol, membrane-associated) in cells transfected with UTP or m^{1}Ψ luciferase IVT mRNAs after sub cellular cell fractionation. Error bars depict s.d. of three biological replicates. High levels of the nuclear U99 in the membrane-associated compartment illustrate successful fractionation. **h**, Western blot analysis of luciferase expression at indicated time points following cycloheximide (CHX) treatment in cells transfected with either UTP or m^{1}Ψ-modified luciferase mRNA. **i**, Quantification of luciferase protein levels normalized to vinculin loading control from panel h. Values are plotted as a function of time post CHX treatment (hours) and fitted to an exponential decay model. Protein half-lives derived from the fitted curves are shown below the graph. **j**, Scatter plots depicting ribosome densities, calculated as the ratio of ribosome footprints to mRNA levels, for human genes (grey) and no uridine in both A and P sites along the spike mRNA (red). The left panel compares cells transfected with UTP or Ψ-modified spike mRNA, and the right panel compares cells transfected with UTP and m^{1}Ψ-modified spike mRNA. **k**, Bar plot showing CCND1 endogenous mRNA levels (control) in input and eIF4E-IP samples from cells transfected with UTP- or m^{1}Ψ-modified luciferase mRNAs, measured by RT-qPCR. Error bars show s.d. of 3 biological replicates. Statistical significance was calculated using linear regression. Fold change between input and IP for each sample is indicated on the graph.

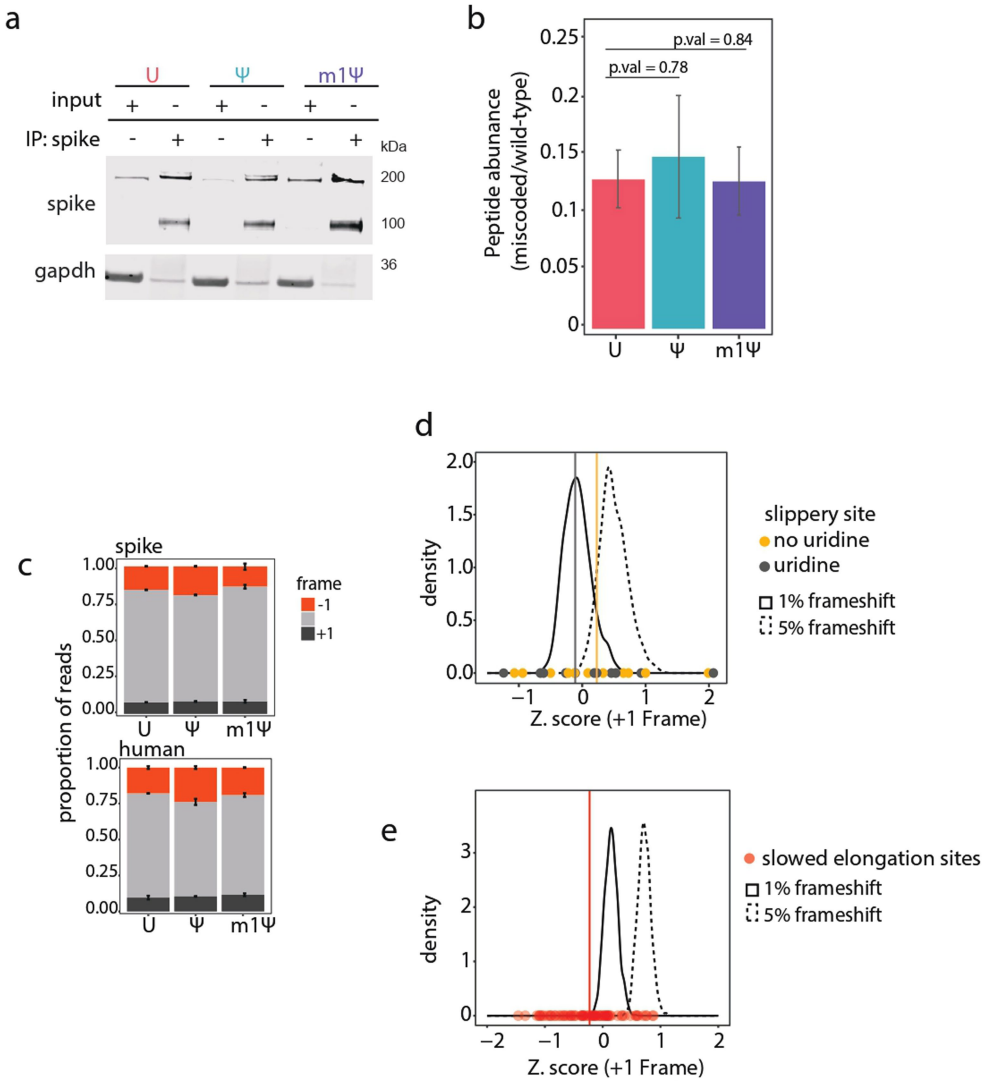

Extended Data Fig. 6 | Slowed elongation on m^{1}Ψ-modified mRNA does not substantially alter translation fidelity or frameshifting. a, Western blot showing immunoprecipitation of Spike protein using anti-Sars-Cov2 spike glycoprotein antibody. Lanes 1,3,5 correspond to input samples and 2,4,6 correspond to immunoprecipitated samples. anti-Gapdh is presented as loading control. **b**, Bar plot depicting mean and s.d. of four biological replicates of peptide abundance measured by mass spectrometry showing the ratio of the intensities of all miscoded spike peptides. P-values were calculated by two sided standard t-test. **c**, Proportion of ribosome footprint reads in each of the 3 reading frames on spike and human mRNAs, averaged for each of the two biological replicates. Error bars show s.d. **d**, The distribution of Z-scores in simulated data enforcing +1 frameshifting, 1% (solid line), 5% (dashed line). The dots depict the computed Z-scores of frame shifting signals from uridine-containing (yellow) or non-uridine-containing (grey) slippery sites. The lines represent the median Z-score of slippery sites in each group. **e**, Density plots of the calculated distributions of median Z. scores for reads mapped to +1 reading frame of simulated data enforcing either 1% (solid line) or 5% (dashed lines) frameshifting. The red dots depicts the observed Z-score of windows downstream to m^{1}Ψ-slowed elongation sites and the red line shows the median value of these scores.

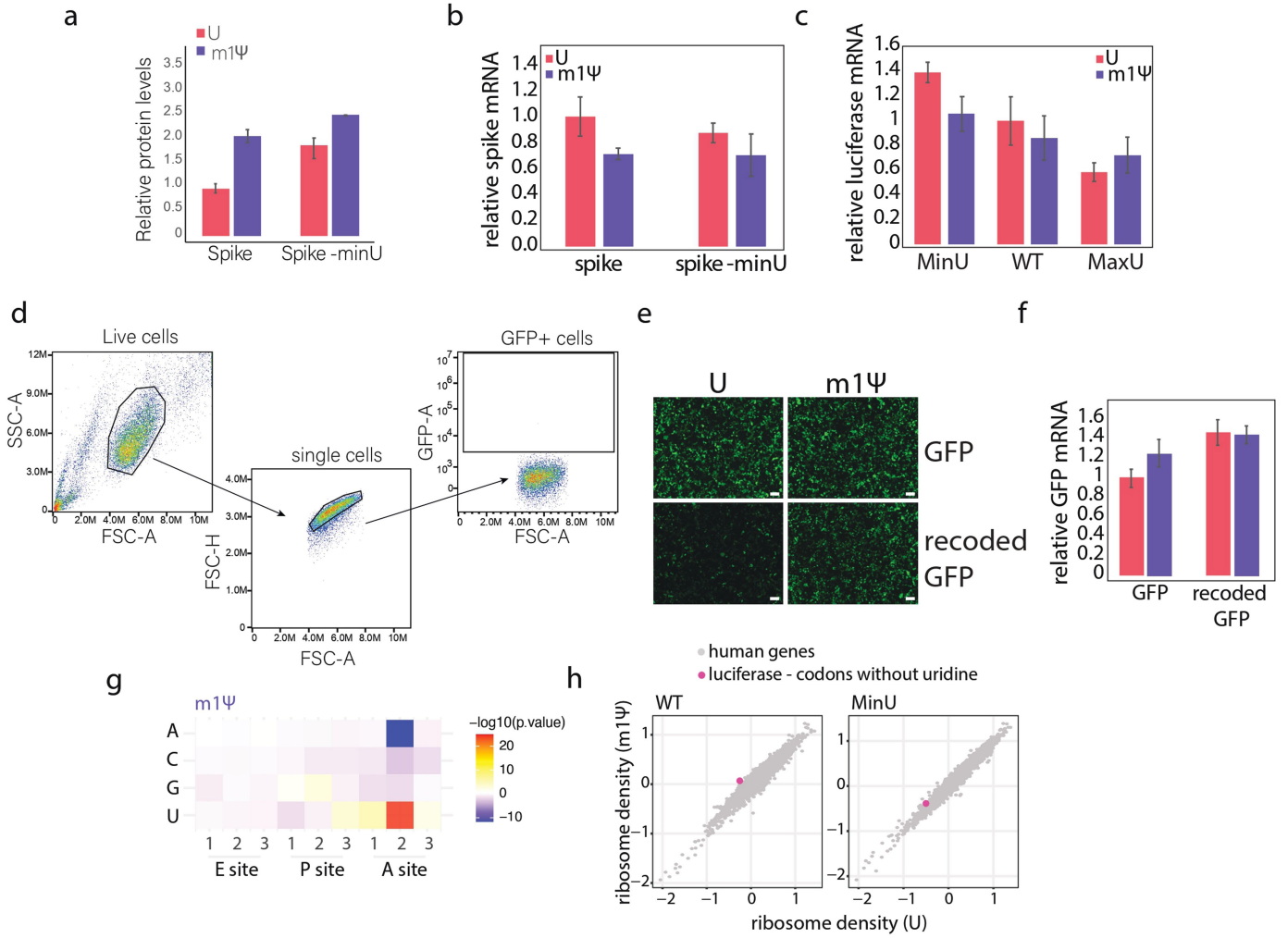

Extended Data Fig. 7 | Synonymous recoding tunes the extent of the m^{1}Ψ-dependent boost in protein expression. a, Bar plots showing Spike protein levels quantified from western blot analysis and normalized to gapdh, in biological duplicates. Error bars show s.d. of duplicates (western blot shown in Fig. 5a). **b**, Average spike mRNA levels for spike and spike-minU UTP or m^{1}Ψ modified mRNA transfected to cells and analysed by RT-qPCR. Gapdh mRNA was used for normalization. Eror bars depict s.d. of two biological duplicates. **c**, Bar plots of average luciferase mRNA levels for UTP or m^{1}Ψ modified luciferase mRNAs; MinU, WT and MaxU analysed by RT-qPCR and normalized to gapdh. Error bars depict s.d. of three biological replicates. **d**, Gating strategy used to determine the live, single-cell, GFP positive population for all flow cytometry analyses of GFP and recoded-GFP. **e**, Microscopy images showing GFP fluorescence in cells transfected with IVT GFP or recoded GFP mRNAs containing either UTP or m^{1}Ψ at 24 h post-transfection ($n = 3$ biologically independent experiments). Representative fields are shown. Scale bar: 100 µm. **f**, Bar plots of relative GFP mRNA levels measured by RT-qPCR and normalized to gapdh for cells transfected with UTP and m^{1}Ψ modified GFP or recoded-GFP mRNAs. Error bars depict s.d. of three biological replicates. **g**, Heatmap depicting -log10 p-values of Fisher exact test of ribosome densities measured for m^{1}Ψ compared to UTP luciferase mRNA for each nucleotide at specific position in the E, A, and P-sites. **h**, Scatter plots depicting ribosome densities, calculated as the ratio of ribosome footprints to mRNA levels in cells transfected with UTP or m^{1}Ψ-modified WT luciferase (left panel) and MinU luciferase (right panel), for human genes (grey) and luciferase mRNA (pink), excluding uridine containing codons.

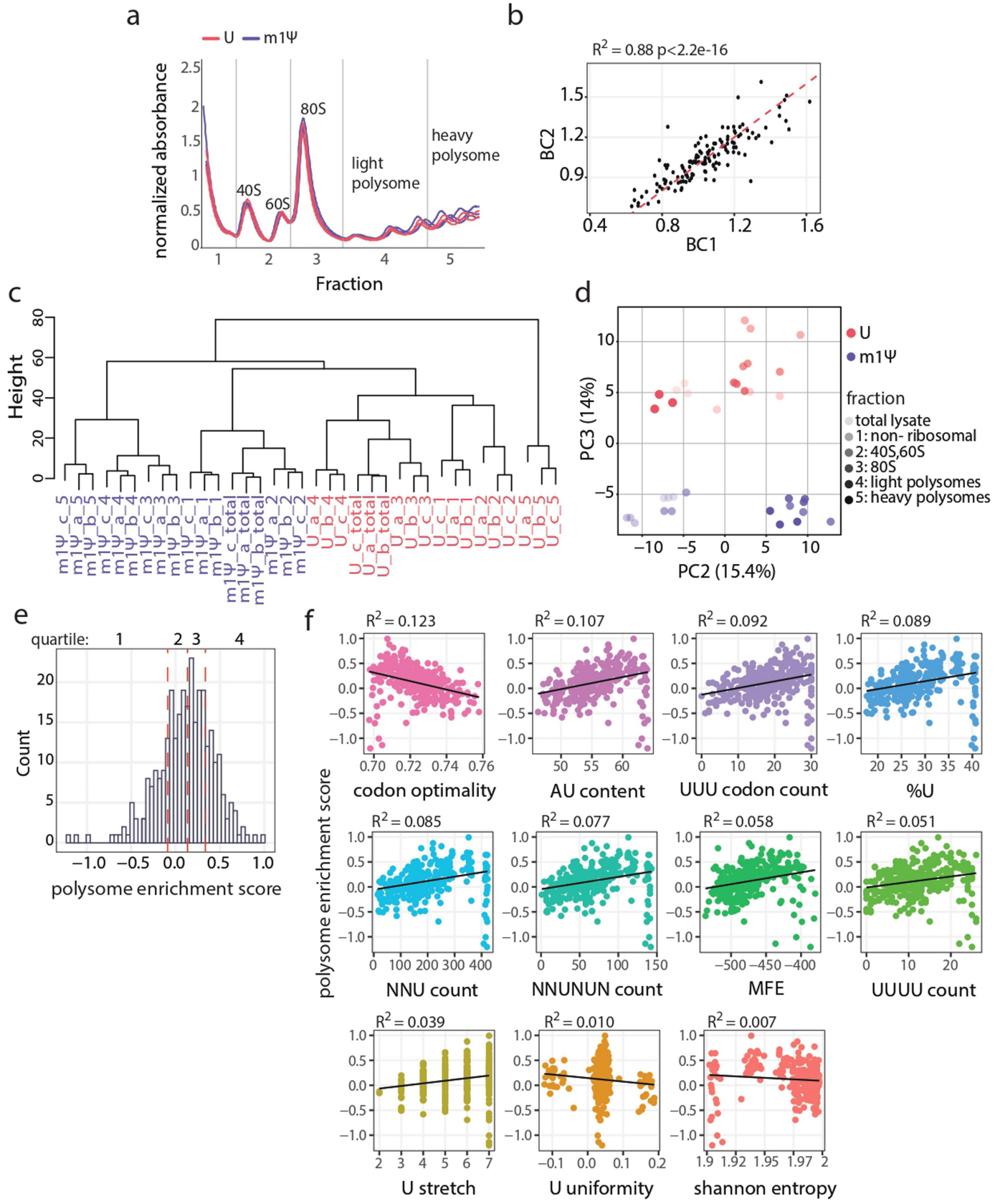

Extended Data Fig. 8 | See next page for caption.

Extended Data Fig. 8 | Quality control of the synonymous luciferase mRNA library. a, Polysome profiles of 293T PKR KO cells transfected with the UTP or $m^1\Psi$ IVT mRNA luciferase mRNA library in biological triplicates normalized to minimum absorbance values. X-axis and grey lines depict the 5 fractions that were collected. **b**, Scatter plot comparing read counts for mRNA sequences with duplicate barcodes (BC1 vs. BC2). Each point represents a sequence, showing high correspondence between barcode replicates ($R^2 = 0.88$, $p < 2.2 \times 10^{-16}$). The red dashed line indicates the linear regression fit. **c**, Dendrogram of hierarchical clustering based on library read counts, showing strong grouping of biological replicates. UTP samples are shown in red and $m^1\Psi$ samples in blue. **d**, Principal component analysis (PCA) of read counts across sequences, shown per sample (UTP-red and $m^1\Psi$-blue), replicate and polysome fraction. Fraction identity is indicated by point shading, ranging from total lysate to non-ribosomal, ribosomal subunits (40S, 60S, 80S), light polysomes, and heavy polysomes. **e**, Histogram showing polysome enrichment score with four quartile cut offs depicted as red dashed vertical lines. **f**, Scatter plots showing the relationship between individual sequence features and the polysome enrichment score. Each point represents a synonymous sequence variant, and the black line indicates the linear regression fit.

Extended Data Table 1 | Cryo-EM data collection, model refinement and validation statistics

	Uridine-PRE (EMD-55091, PDB-9SPI)	$m^1\Psi$-PRE (EMD-55083, PDB-9SPF)
Data collection and processing		
Microscope	Titan Krios	Titan Krios
Camera	Gatan K3	Gatan K3
Voltage (kV)	300	300
Magnification	105000	105000
Pixel size (Å)	0.8245	0.8245
Defocus range (μM)	(-0.6) - (-1.7)	(-0.6) - (-1.7)
Total electron exposure (e/Å^2)	41.42	43.07
Micrographs collected	35660	29926
Symmetry imposed	C1	C1
Number of particles (autopicked)	1895998	3076448
Number of particles (used for 3D reconstruction)	94974	121901
Map resolution (Å)	2.4	2.4
FSC threshold	0.143	0.143
CC (model to map fit)	0.84	0.91
Refinement		
Initial model used (PDB code)	8GLP	8GLP
Map sharpening *B* factor (Å^2)	-25	-20
Model composition		
Non-hydrogen atoms	216692	211465
Protein residues	11071	11325
Nucleotides	5447	5566
Ligands		
PUT	8	9
ZN	7	7
HYG	1	1
K	75	151
SPD	18	19
MG	195	225
NA	-	35
R.M.S. deviations		
Bond lengths (Å)	0.004	0.009
Bond angles (°)	0.795	1.049
Chirality (˚)	0.052	0.114
Planarity (˚)	0.005	0.011
Validation		
Clashscore	6.75	4.99
MolProbity score	1.72	1.67
Rotamer outliers (%)	2.45	2.41
Ramachandran plot		
Favored (%)	97.76	97.4
Allowed (%)	2.18	2.56
Disallowed (%)	0.06	0.04
RNA		
Correct sugar pucker (%)	99.69	99.48
Correct backbone conformation (%)	88.57	84.95

Summary of cryo-EM data collection parameters, reconstruction metrics, model refinement, and validation statistics for the uridine–PRE and $m^1\Psi$–PRE complexes.